

University of Windsor

Scholarship at UWindor

Electronic Theses and Dissertations

Theses, Dissertations, and Major Papers

2013

A Preliminary Study on Intake Flow to Improve In-Cylinder Air Motion

Qiaochu Han
University of Windsor

Follow this and additional works at: <https://scholar.uwindsor.ca/etd>

Recommended Citation

Han, Qiaochu, "A Preliminary Study on Intake Flow to Improve In-Cylinder Air Motion" (2013). *Electronic Theses and Dissertations*. 4873.

<https://scholar.uwindsor.ca/etd/4873>

This online database contains the full-text of PhD dissertations and Masters' theses of University of Windsor students from 1954 forward. These documents are made available for personal study and research purposes only, in accordance with the Canadian Copyright Act and the Creative Commons license—CC BY-NC-ND (Attribution, Non-Commercial, No Derivative Works). Under this license, works must always be attributed to the copyright holder (original author), cannot be used for any commercial purposes, and may not be altered. Any other use would require the permission of the copyright holder. Students may inquire about withdrawing their dissertation and/or thesis from this database. For additional inquiries, please contact the repository administrator via email (scholarship@uwindsor.ca) or by telephone at 519-253-3000ext. 3208.

A Preliminary Study on Intake Flow to Improve In-Cylinder Air Motion

by

Qiaochu Han

A Thesis
Submitted to the Faculty of Graduate Studies
through the Department of Mechanical, Automotive, and Materials Engineering
in Partial Fulfillment of the Requirements for
the Degree of Master of Applied Science at the
University of Windsor

Windsor, Ontario, Canada

2013

© 2013 Qiaochu Han

A Preliminary Study on Intake Flow to Improve In-Cylinder Air Motion

by

Qiaochu Han

APPROVED BY:

Dr. Xiaohong Xu, Outside Department Reader
Department of Civil and Environmental Engineering

Dr. Jimi Tjong, Department Reader
Department of Mechanical, Automotive, and Materials Engineering

Dr. Ming Zheng, Advisor
Department of Mechanical, Automotive, and Materials Engineering

Dr. David Ting, Advisor
Department of Mechanical, Automotive, and Materials Engineering

23 April 2013

DECLARATION OF ORIGINALITY

I hereby certify that I am the sole author of this thesis and that no part of this thesis has been published or submitted for publication.

I certify that, to the best of my knowledge, my thesis does not infringe upon anyone's copyright nor violate any proprietary rights and that any ideas, techniques, quotations, or any other material from the work of other people included in my thesis, published or otherwise, are fully acknowledged in accordance with the standard referencing practices. Furthermore, to the extent that I have included copyrighted material that surpasses the bounds of fair dealing within the meaning of the Canada Copyright Act, I certify that I have obtained a written permission from the copyright owner(s) to include such material(s) in my thesis and have included copies of such copyright clearances to my appendix.

I declare that this is a true copy of my thesis, including any final revisions, as approved by my thesis committee and the Graduate Studies office, and that this thesis has not been submitted for a higher degree to any other University or Institution.

ABSTRACT

The intake flow of a diesel engine significantly affects the combustion characteristics, thus influencing the power output, fuel efficiency and the emissions. In this thesis work, simulations using computational fluid dynamics (CFD) along with steady flow experiments were conducted to study the intake flow of a Yanmar NFD-170 diesel engine. The in-cylinder air motion generated by the intake flow through the helical intake port was studied. In order to model the shape of the engine accurately, a three dimensional model of the engine intake port, cylinder head and cylinder was produced using AutoDesk Inventor. The air motion was simulated under steady flow conditions using Converge CFD software, and the simulation results were compared with the experimental results to validate the model. The results indicated that major features of the steady flow were well modeled at particular flow conditions.

DEDICATION

To my parents with all my heart.

ACKNOWLEDGEMENTS

I would like to thank my thesis advisors, Dr. Ming Zheng and Dr. David Ting for the motivation, the direction and the guidance they provided, without which this work would have been impossible.

I would like to thank my thesis committee members, Dr. Xiaohong Xu, Dr. Jimi Tjong and the Chair of Defence, Dr. Andrzej Sobiesiak, for giving me constructive criticism and helping me improve my thesis.

I am also grateful to all of my current and former colleagues at the Clean Diesel Laboratory at the University of Windsor: Dr. Meiping Wang, Dr. Shui Yu, Xiaoye Han, Kelvin Xie, Tongyang Gao, Dr. Tadanori Yanai, Prasad Divekar, Shouvik Dev, Marko Jestic, Qingyuan Tan and Geraint Bryden.

Ultimately, I would like to thank my parents for their support, their help and their guidance in every step of my life.

TABLE OF CONTENTS

DECLARATION OF ORIGINALITY	iii
ABSTRACT.....	iv
DEDICATION	v
ACKNOWLEDGEMENTS	vi
LIST OF TABLES.....	ix
LIST OF FIGURES	x
NOMENCLATURE	xii
CHAPTER 1 INTRODUCTION	1
1.1 Background.....	1
1.2 Numerical simulation.....	3
1.3 Transient process	3
1.5 Laser Doppler Anemometry (LDA).....	7
1.6 Particle Image Velocimetry (PIV)	9
1.7 Layout of the thesis.....	10
CHAPTER 2 SIMULATION SETUP	12
2.1 Surface preparation in a graphical pre-processor.....	13
2.2 Input files specification.....	14
2.2.1 Solver	14
2.2.2 Boundary conditions	16
2.3 Calculation and post-processing	23
CHAPTER 3 EMPIRICAL SETUP AND OPERATING CONDITIONS	25
3.1 Empirical setup	25
3.2 Operating conditions.....	29
CHAPTER 4 RESULTS AND DISCUSSION.....	30
4.1 Transient Yanmar NFD-170 engine model simulation results	30
4.2 Steady state model simulation results	32
4.3 Steady state experimental results	47

4.4 Comparison of model predictions and measurements	54
4.5 Limitations of steady state flow	60
CHAPTER 5 CONCLUSION.....	61
REFERENCES	63
APPENDIX A CONVERGE SIMULATION INPUT FILES LIST.....	65
APPENDIX B MATLAB CODES FOR CONTOUR PLOTS.....	66
APPENDIX C MATLAB CODES FOR QUIVER PLOTS	68
VITA AUCTORIS	70

LIST OF TABLES

Table 1 Geometrical characteristics of Yanmar NFD-170 engine.....	20
Table 2 Simulation conditions for the Yanmar NFD-170 engine model.....	23
Table 3 Simulation conditions for the steady state model	23
Table 4 Experiment condition.....	29
Table 5 Average mass flow rate of different engine speeds	31
Table 6 Increments on mass flow rates and average intake air velocity	44
Table 7 Property of measured planes.....	49

LIST OF FIGURES

Figure 1 Swirl and tumble structure.....	2
Figure 2 Valve lift profile of intake process	4
Figure 3 Effective flow area	5
Figure 4 An example of in-cylinder air motion	6
Figure 5 LDA operating principle.....	8
Figure 6 A typical PIV setup [13].....	9
Figure 7 Schematic of the CONVERGE file interaction	12
Figure 8 Graphical pre-processor: CONVERGE UI.....	14
Figure 9 Flow chart of CONVERGE simulation	16
Figure 10 Yanmar NFD-170 engine model	17
Figure 11 Steady state model.....	18
Figure 12 Valve lift profile of Yanmar engine model and steady state model	18
Figure 13 Intake valve lift position of steady state model	19
Figure 14 Boundary conditions and regions of Yanmar NFD-170 engine model	20
Figure 15 Boundary conditions and regions of the steady state model.....	21
Figure 16 Inflow and outflow direction of the steady state model	22
Figure 17 Geometry of the cylinder and the Yanmar NFD-170 cylinder head.....	25
Figure 18 Experiment setup.....	26
Figure 19 Schematic diagram of the experiment setup.....	27
Figure 20 5W argon gas laser	28
Figure 21 Point-by-point velocity measurement.....	28
Figure 22 Mass flow rate vs. crank angle	31
Figure 23 Average mass flow rate calculation.....	31
Figure 24 Average mass flow rate vs. engine speed	32
Figure 25 Mean RMS velocity at different mass flow rates	33
Figure 26 Turbulence kinetic energy at equivalent engine speeds	34
Figure 27 Positions of the selected analysis planes	35
Figure 28 Velocity vectors in XZ plane with mass flow rate of 45 g/s	37
Figure 29 Magnitude velocity in XZ plane with mass flow rate of 45 g/s.....	37
Figure 30 Velocity vectors in XY plane with mass flow rate of 45 g/s.....	38
Figure 31 Magnitude velocity in XY plane with mass flow rate of 45 g/s	38
Figure 32 Velocity vectors in XZ plane with mass flow rate of 41.5 g/s	39
Figure 33 Magnitude velocity in XZ plane with mass flow rate of 41.5 g/s.....	40
Figure 34 Velocity vectors in XY plane with mass flow rate of 41.5 g/s	40
Figure 35 Magnitude velocity in XY plane with mass flow rate of 41.5 g/s	41
Figure 36 Velocity vectors in XZ plane with mass flow rate of 36.5 g/s	42
Figure 37 Magnitude velocity in XZ plane with mass flow rate of 36.5 g/s.....	43
Figure 38 Velocity vectors in XY plane with mass flow rate of 36.5 g/s	43
Figure 39 Magnitude velocity in XY plane with mass flow rate of 36.5 g/s	44
Figure 40 Velocity vectors in XZ plane with mass flow rate of 4 g/s	45
Figure 41 Magnitude velocity in XZ plane with mass flow rate of 4 g/s.....	46
Figure 42 Velocity vectors in XY plane with mass flow rate of 4 g/s.....	46

Figure 43 Magnitude velocity in XY plane with mass flow rate of 4 g/s	47
Figure 44 Positions of selected XY planes	49
Figure 45 Position of selected XZ plane	50
Figure 46 Average mass flow rate at different engine speeds	51
Figure 47 Velocity vectors in z=8 mm plane	52
Figure 48 Velocity vectors in z=25 mm plane	52
Figure 49 Velocity vectors in z=50 mm plane	53
Figure 50 Velocity vectors in the center XZ plane of the cylinder	54
Figure 51 Comparison of measured and computed velocity vectors in z=8 mm plane	56
Figure 52 Comparison of measured and computed velocity vectors in z=25 mm plane	57
Figure 53 Comparison of measured and computed velocity vectors in z=50 mm plane	58
Figure 54 Comparison of measured and computed velocity vectors in the XZ plane	59
Figure 55 A comparison of intake port pressure between steady flow and transient flow	60

NOMENCLATURE

A	the total area of the inflow/outflow surface
A_v	valve area
BDC	bottom dead center
CA	crank angle
CCD	charge-coupled device
CFD	computational fluid dynamics
LDA	laser Doppler anemometry
PIV	planar image velocimetry
P_o	upstream stagnation pressure
P_v	valve static pressure
P_{avg}	average density at the boundary surface
TDC	top dead center
TKE	turbulence kinetic energy
U	mean velocity component in x-direction
V	mean velocity component in y-direction
W	mean velocity component in z-direction
c_f	flow coefficient
c_o	stagnation speed of sound
d_f	fringe spacing
f_D	Doppler frequency
n_i	the outward pointing surface normal
U	the velocity component at x axis
V	the velocity component at y axis
W	the velocity component at z axis
ρ_o	stagnation density
Λ	wave length
Θ	angle between two laser light

CHAPTER 1

INTRODUCTION

1.1 Background

A main goal of an internal combustion engine is to exhibit good performance while meeting the stringent emission standards. In the past decades, diesel engines have been greatly improved in terms of the engine efficiency and pollutant emissions and this trend will continue. In recent years, demanding emission requirements were established by governing authorities. In order to meet those requirements, the outcomes of the combustion process are very important in internal combustion engines. Moreover, the combustion is affected by the in-cylinder air motion. It is well known that the intake process governs many important aspects of the air motion within the cylinder. The structures of the in-cylinder flow are complex. Therefore, a thorough understanding of the in-cylinder air motion is necessary to improve the performance of internal combustion engines.

There are two parameters that can be used to characterize the in-cylinder air motion, i.e. the swirl and the tumble. The swirl is described as the rotational air motion with respect to the cylinder axis. The swirl is generated during the air induction into the cylinder by either directing the flow into the cylinder tangentially or pre-swirling the incoming flow with helical ports. The rotation which occurs with respect to the axis perpendicular to the cylinder axis is called tumble. The general structure of the swirl and tumble is shown in Figure 1.

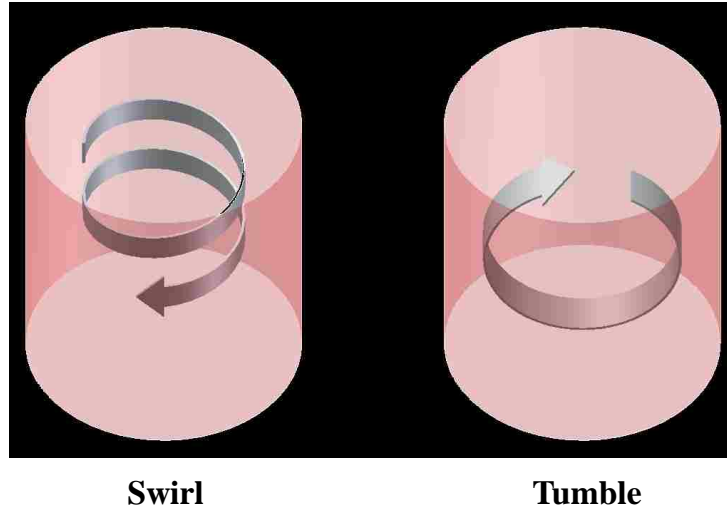


Figure 1 Swirl and tumble structure

Typically, the swirl and tumble are generated during the intake process to improve the mixing and to create a high turbulence level at the compression top dead center. This introduces the opportunity to control the combustion process and consequently control the burning efficiency and emissions by modifying the in-cylinder flow. However, it is not always straightforward to define the most advantageous flow structure. Furthermore, the complex flow processes also strongly depend on the specific characteristics of a particular engine.

A good understanding and the ability to predict and control the in-cylinder air motion are very important in developing engines to meet the current and future emission requirements. However, the nature of the engine working processes makes the in-cylinder flow difficult to quantify. Many researchers have studied the intake flow and in-cylinder air motion in internal combustion engines using various methods [3, 4, 6, 9, 10]. These include numerical simulations and experimental techniques, such as the particle planar image velocimetry (PIV), laser Doppler anemometry (LDA) and the steady flow bench.

1.2 Numerical simulation

Unlike other methods, the numerical simulation modeling provides an opportunity to generate the detailed flow information of the entire flow field which may be difficult to attain from experimental approaches. To extend the understanding of the in-cylinder air motion, the flow can be simulated using computational fluid dynamics. The numerical simulation modeling of the in-cylinder flow using computational fluid dynamics has become popular in the recent decades. In the past, the three dimensional calculation codes were used to solve the governing equations and to generate velocity distributions and mean velocities. The codes usually required a long time to complete the calculation and the available computing power was limited. However, these problems are partially solved in recent years owing to the significant improvement of the simulation software and the improved performance of modern computers.

1.3 Transient process

A system is in a transient state when a process variable has been changed and the system has not yet reached a steady state [2]. In the engine intake process, the intake valve starts to open before the top dead center (TDC) and then fully closes after the bottom dead center (BDC). Figure 2 shows an example of the intake valve lift profile during this process.

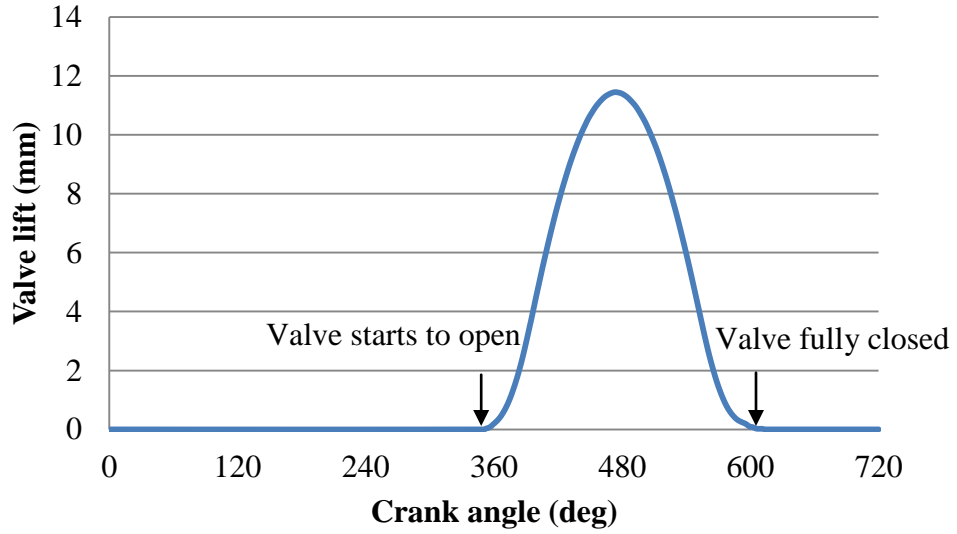


Figure 2 Valve lift profile of intake process

The mass flow rate through the valve is also related to the valve lift [7], and the mass flow rate can be estimate by:

$$\dot{m} = c_f \rho_o A_v c_o \left[\frac{2}{k-1} \left(\left(\frac{P_v}{P_o} \right)^{\frac{2}{k}} - \left(\frac{P_v}{P_o} \right)^{\frac{k+1}{k}} \right) \right]^{\frac{1}{2}} \quad (1)$$

where,

\dot{m} = mass flow rate

P_o = upstream stagnation pressure

P_v = valve static pressure

ρ_o = stagnation density

$c_o = \sqrt{kRT_o}$ stagnation speed of sound

k = specific heat ratio

R = molar gas constant

T = absolute temperature in kelvin

A_v = valve area

c_f = flow coefficient

The intake flow is in practice a transient process because of the motion of the valves, the motion of the piston, and the effects of the pressure. The pressure in the intake manifold typically drops during the air induction process. Furthermore, the pulsations of the pressure incurred by the intermittent action of the valves induce complexes to the flow process.

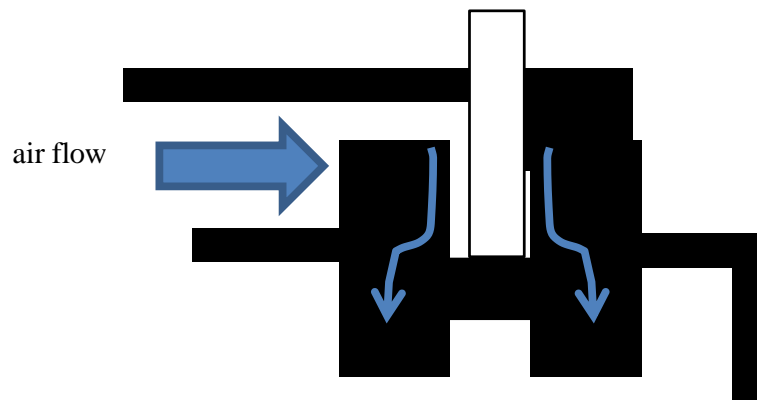


Figure 3 Effective flow area

From this point of view, the engine is operating under transient conditions. As the valve opens, the air will flow into the cylinder, and thereby forming the air motion. Figure 4 shows an example of the magnitude of the air velocity for two different horizontal planes inside a cylinder during the intake process.

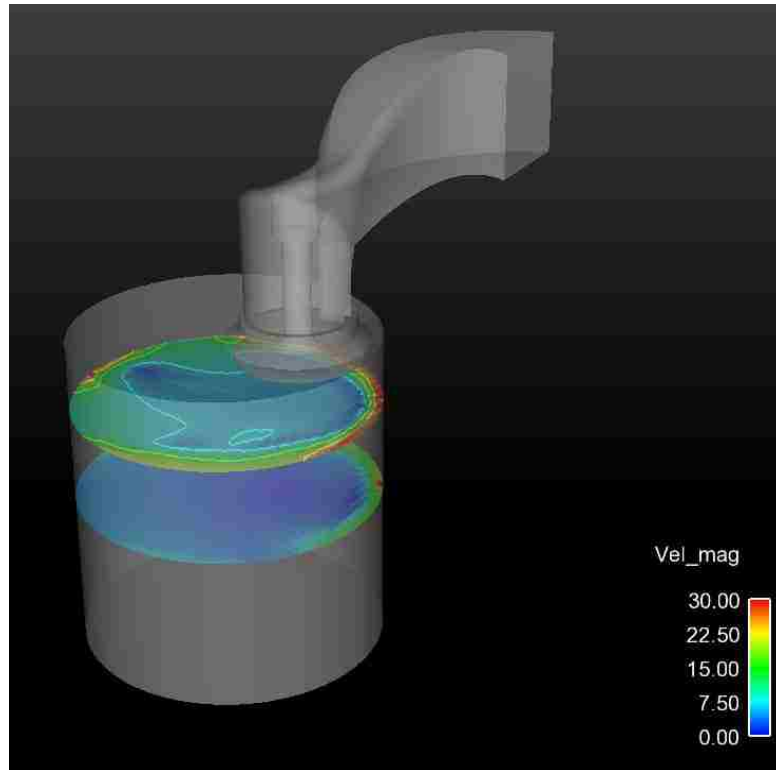


Figure 4 An example of in-cylinder air motion

1.4 Steady state

A steady state henceforth refers to a stable condition that does not change over time or in which the change in one direction is continuously balanced by the change of another. This implies that for any property p of the system, the partial derivative with respect to time is zero [1]:

$$\frac{\partial p}{\partial t} = 0 \quad (2)$$

Ultimately, the verification should be carried out on the unsteady in-cylinder flow problem since only transient analysis can yield detailed information on the flow field during the intake process. Because of the complexity of this problem, from both

computational and experimental point of view, the preliminary verification is usually performed on the steady flow bench [9].

The steady state measurement is a simplified design tool to study the performance of an engine. In recent years, testing on the steady flow bench has been a standard method to characterize the in-cylinder air motion in the automotive industry. The main assumption of this method is that there is a close correspondence between the steady state measurements and those that would be obtained from a cylinder of a running engine. Most of the work is performed under steady flow conditions for several reasons. First, this work is usually required to obtain a general idea at the early stage of the design before a complete engine is built. Second, it is much simpler to set up the steady state system and easier to do the measurements. Third, it is more efficient in time and cost to perform.

1.5 Laser Doppler Anemometry (LDA)

Since the first LDA measurement was successfully tested e.g. by Yeh and Cummins (1964), the method has been undergoing continuous development [11]. The LDA is the technique of using the Doppler shift in a laser beam to measure the velocity [12]. It is an optical method and hence tightly related to both the physical and geometrical optics. It is a widely accepted tool for investigating fluid dynamics with gases and liquid, and it has been used as such for more than three decades.

As the fluid moves through the probe volume with tiny seeding particles, the information of the flow velocity is generated. When a particle passes through the intersection volume formed by the two coherent laser beams, the scattered light, received by a detector, has

components from both beams. Figure 5 describes the LDA operating principle. The fringe spacing, d_f , is defined as

$$d_f = \frac{\lambda}{2 \sin\left(\frac{\theta}{2}\right)} \quad (3)$$

where,

λ is the wave length

θ is the angle between two laser beams

The seeding particle takes time $t=1/f_D$, where f_D is the Doppler frequency, to create one fringe. The distance between the fringes divided by time gives the magnitude of the velocity of the seeding particle in the measurement plane. Hence,

$$V = \frac{d_f}{t} = d_f \times f_D \quad (4)$$

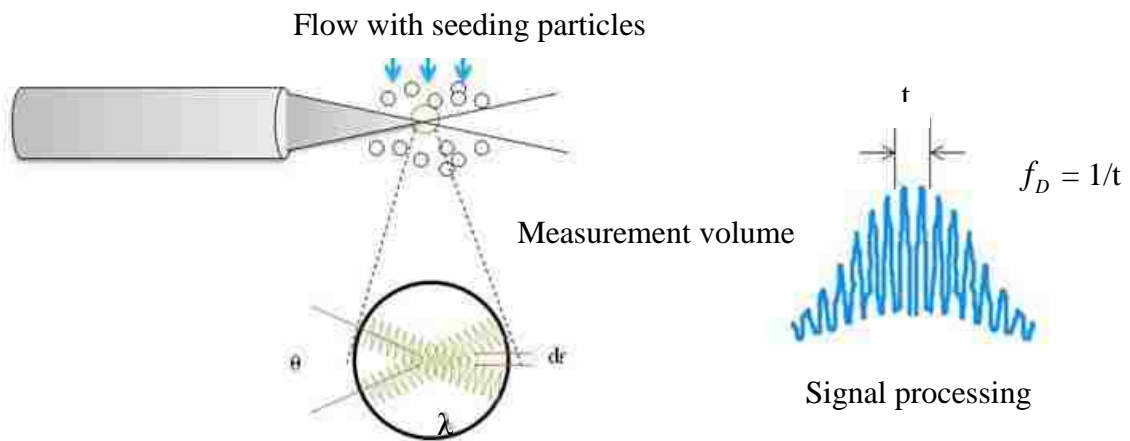


Figure 5 LDA operating principle

1.6 Particle Image Velocimetry (PIV)

The particle image velocimetry (PIV) is a whole-flow-field technique providing instantaneous velocity vector measurements on a cross sectional plane of a flow [16]. A typical PIV setup is shown in Figure 6; it contains a charge-coupled device (CCD) camera, a high power laser, and an optical system to convert the laser output light to a light sheet, tracer particles and a control system to synchronize the laser output with the camera image acquisition.

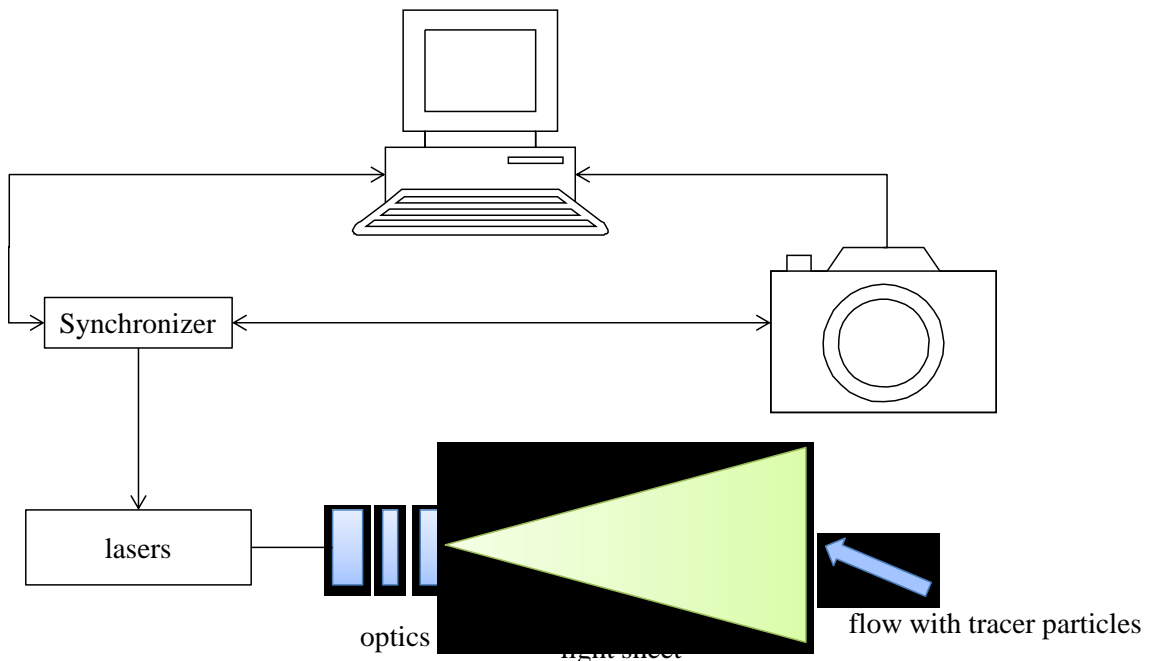


Figure 6 A typical PIV setup [13]

This technique is applicable to a range of liquid and gaseous flows. In order to capture the flow, the fluid is seeded with particles. The optical system is configured to produce a thin sheet of light in the measurement plane. Two consecutive images of the measurement plane would capture the seeding particles at different positions. The particle displacement and the frame traveled by an individual particle within this time period can

be calculated. The velocity field is generated by dividing the displacement field by the known time separation.

There are also some limitations of PIV [13]:

- 1) The time interval between the laser pulses needs to be properly scheduled to capture a distinctive displacement of the seeding particles.
- 2) The size of the seeding particles is important. When the particles can follow the flow properly, the accuracy of the PIV measurements can be improved dramatically. Smaller sized particles can be used when a higher power laser is applied.
- 3) It is required that the integral area should be small to avoid significant velocity gradient within this area.

1.7 Layout of the thesis

The thesis study focuses on the numerical analysis for both complete engine in-cylinder flow and the steady state flow. The experimental analysis of the steady state flow is also conducted. This thesis investigates the flow through a Yanmar NFD-170 engine cylinder head using both numerical and experimental techniques. A commercial simulation software package, CONVERGE, is used to investigate the flow structure inside an engine cylinder. Chapter 2 documents the details of the simulation setup and general procedures. The experiments focus on determining the distribution of velocities in the cylinder under the steady state conditions at different intake mass flow rates. The details related to the experiment design and the LDA setup are provided in Chapter 3. The LDA technique was used to perform the experimental analysis. Subsequently, the results of both numerical simulations and experimental measurements are presented in Chapter 4. The in-cylinder

air flow structures and mean velocities are also discussed in Chapter 4. The conclusions are summarized in the final chapter.

CHAPTER 2

SIMULATION SETUP

The CONVERGE simulation package is a simulation software that can simulate three-dimensional, compressible or incompressible, and chemically reacting transient fluid flows in complex geometries with stationary or moving surfaces [8]. It is an extremely powerful tool for rapidly and accurately simulating all internal combustion engine types.

Figure 7 shows a schematic of the file interaction with CONVERGE.

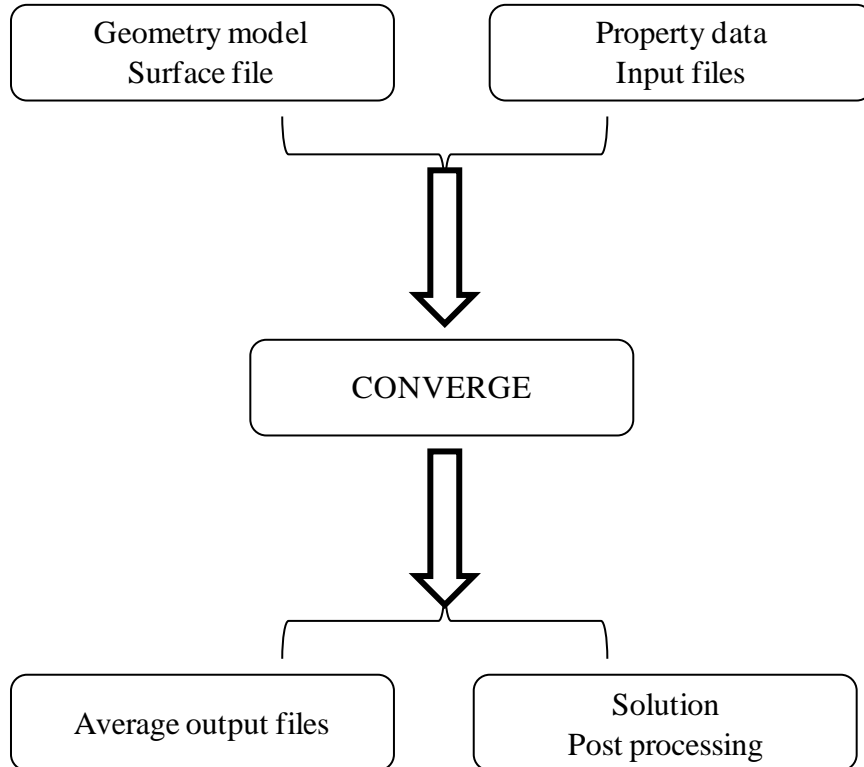


Figure 7 Schematic of the CONVERGE file interaction

This workflow can be split into four steps:

- (1) Surface preparation in a graphical pre-processor
- (2) Input files specifications (initial and boundary conditions)

- (3) Calculation
- (4) Post processing

The following sections will provide details of each step.

2.1 Surface preparation in a graphical pre-processor

In order to run a simulation in CONVERGE, efforts must be made to prepare the geometry surface and the input files that control the simulation.

A Stereolithography (STL) format file containing the surface of the geometry is required to import into CONVERGE, which can be easily generated from most CAD packages. After importing the geometry, a graphical user interface pre-processor is used to prepare and export the surface definition file, which is one of the input files for the CONVERGE solver. This user interface is called CONVERGE UI, which is shown in Figure 8. The geometry of the surface with unique boundary regions is identified in the surface definition file and the volume mesh is created automatically during the runtime by the CONVERGE solver.

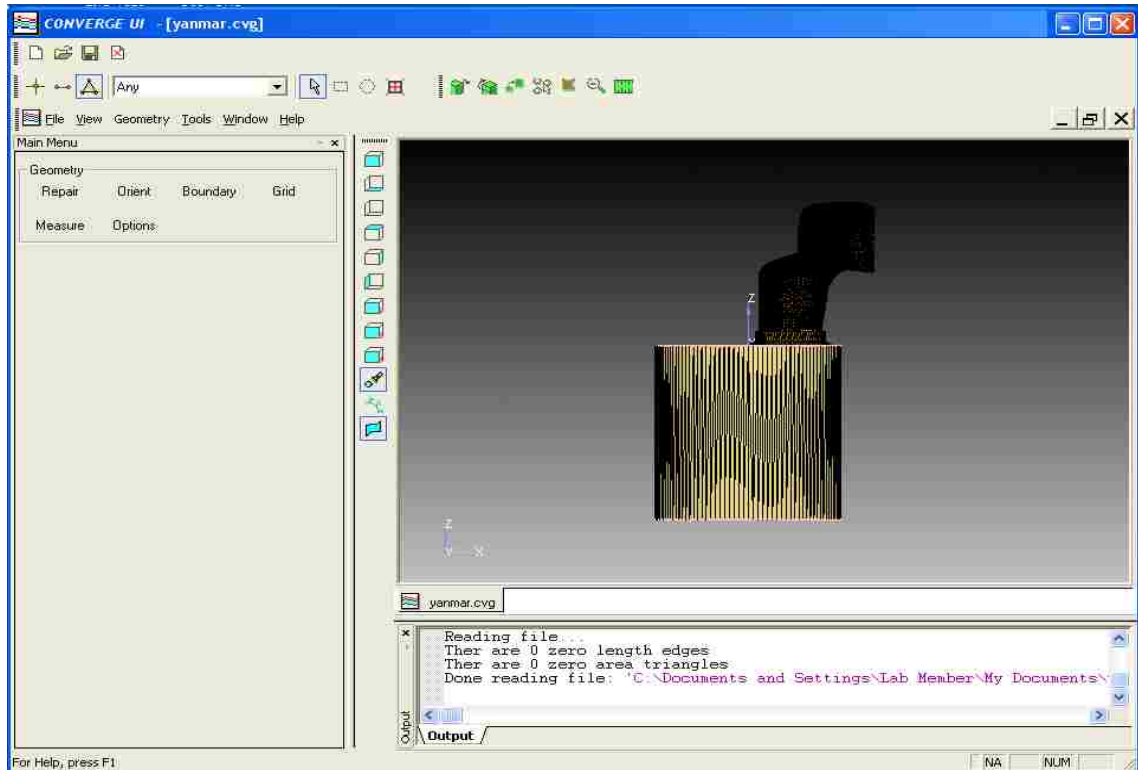


Figure 8 Graphical pre-processor: CONVERGE UI

The CONVERGE package uses an innovative boundary approach that eliminates the need for the computational grid to coincide with the geometry of interest. There are many benefits of generating the grid internally to the code at run time. First, it allows the grid to change during the simulation. Second, it can handle moving surfaces by regenerating the grid near the moving boundaries without having specified input files. Finally, it offers significant time saving over other CFD codes.

2.2 Input files specification

2.2.1 Solver

There are two types of solvers in CONVERGE: the transient solver and the steady state solver. The transient solver is used to run the Yanmar NFD-170 engine model with different engine speeds. In a transient case, the transport equation is given as

$$\frac{\partial \rho \varphi}{\partial t} + \frac{\partial \rho u_i \varphi}{\partial x_i} = \frac{\partial}{\partial x_i} \left(\rho D \frac{\partial \varphi}{\partial x_i} \right) + S \quad (5)$$

where φ is any transported variable.

The experiments are done under steady state conditions. Because of this, the steady state solver is selected to run the experiment model. By definition, the solution of a steady case does not change with time. So the derivative term that depends on time is removed from the transport equation for the steady state. Transport equation for steady state is given as

$$\frac{\partial \rho u_i \varphi}{\partial x_i} = \frac{\partial}{\partial x_i} \left(\rho D \frac{\partial \varphi}{\partial x_i} \right) + S \quad (6)$$

The steady state simulation does not require inputs in absolute time, and thus the time based inputs that control the start time, end time, etc. are given in cycles instead of time (seconds). A cycle is a completion of the algorithm shown in Figure 9. At the start of each cycle, the previous values are stored and explicit sources are calculated for each sub-model. At the beginning of the computation iterations, only momentum, pressure and velocity are solved. It is necessary to check the convergence after each iteration. The iterations will continue until the convergence is achieved. Another iteration, which is defined as “strict conserve” by CONVERGE, is added after the computation iterations convergence to improve the results.

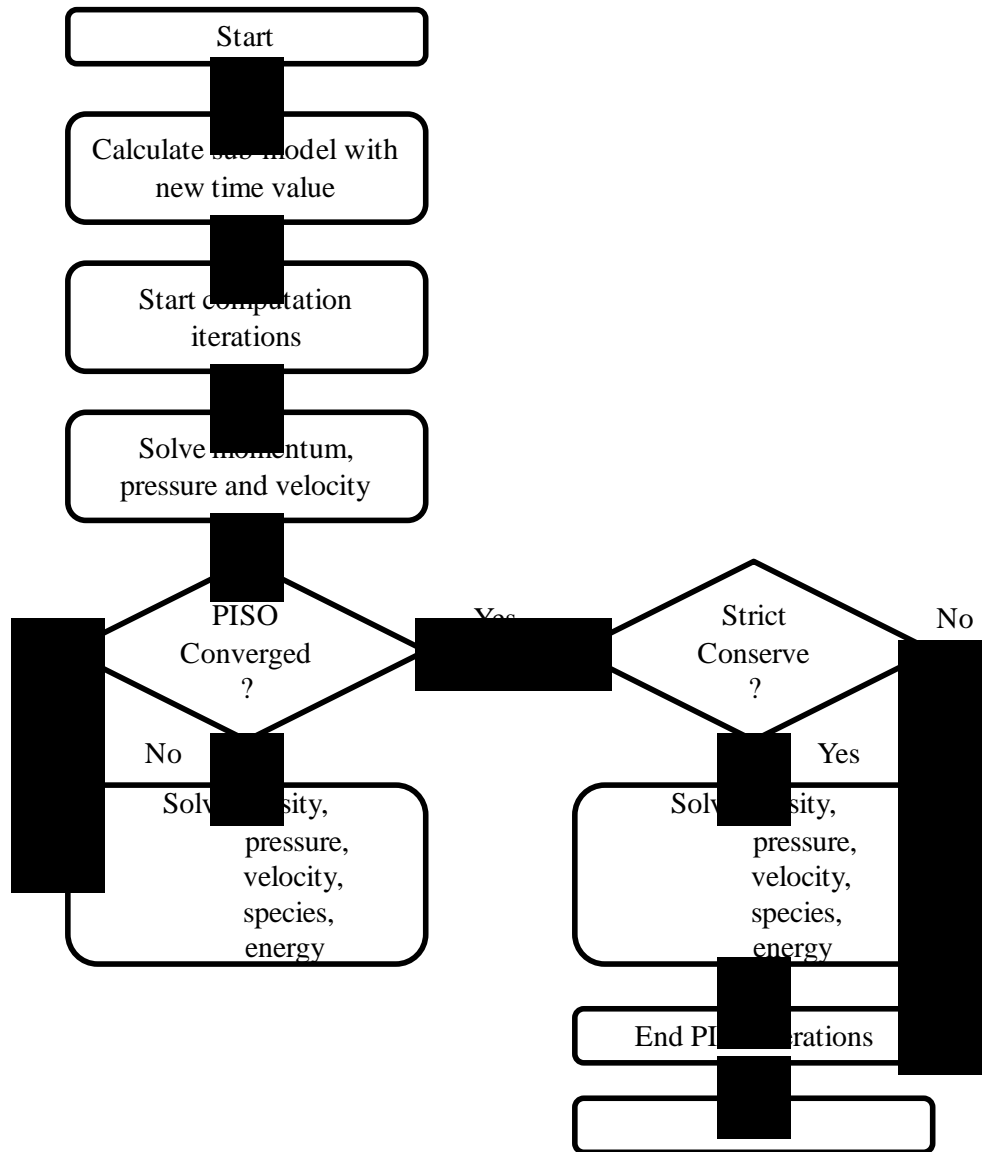


Figure 9 Flow chart of CONVERGE simulation

2.2.2 Boundary conditions

The boundary conditions are similar between the transient and steady state models. One of the main differences is that instead of having a moving piston, the steady state model is equipped with an open end cylinder, as shown in Figure 10 and Figure 11. Another difference is the initial intake valve position and the intake valve profile. Figure 12 shows the intake valve profile of the Yanmar NFD-170 engine model and the steady state model. As shown in Figure 12, the intake valve of the Yanmar NFD-170 engine model opens at

-363°CA and closed at -121°CA during the simulation procedure. In order to have a better correlation between these two models, the intake valve lift for the steady state model is set to a fix position based on the Yanmar engine model valve lift profile. The average valve lift of the Yanmar engine is about 5.6 mm during the intake process. As an attempt to be representative, the intake valve lift of the steady state model is set at 6 mm for all cases, as indicated in Figure 13.

The fluid for both of the Yanmar NFD-170 engine model and the steady state model is air. The air temperature is specified as 298 K and the composition of the mixture is defined as 23% oxygen with 77% nitrogen by mass. The density of air is calculated by the ideal gas law.

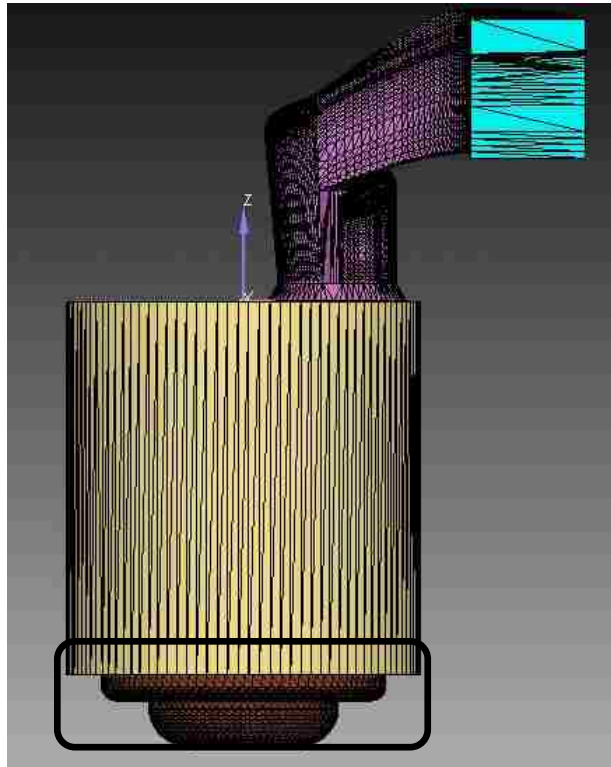


Figure 10 Yanmar NFD-170 engine model

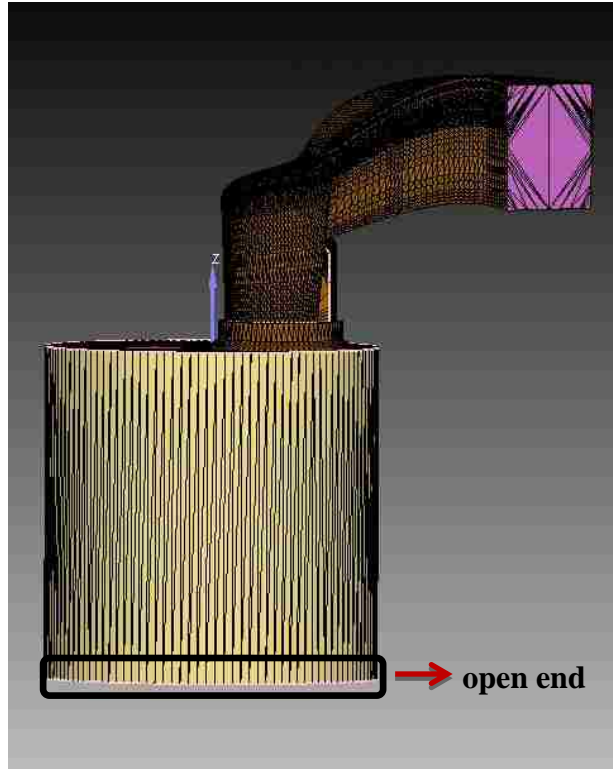


Figure 11 Steady state model

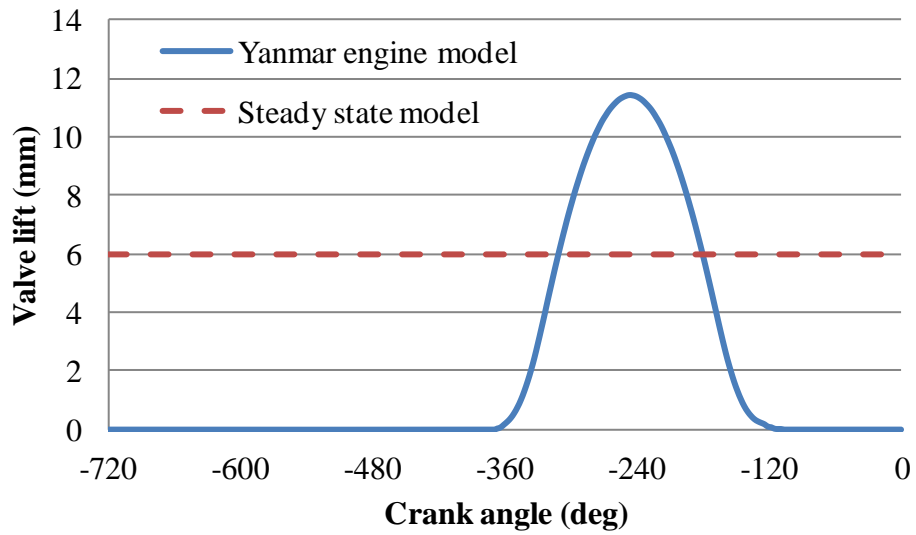


Figure 12 Valve lift profile of Yanmar engine model and steady state model

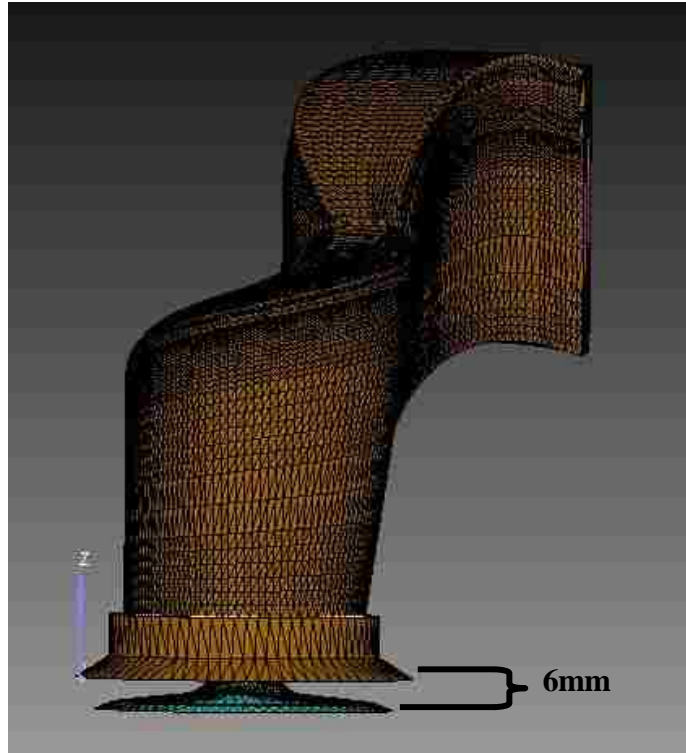


Figure 13 Intake valve lift position of steady state model

There are eight sets of boundary conditions defined in the transient Yanmar NFD-170 engine model, which are separated into two regions, as shown in Figure 14. Region 0 contains the piston, the cylinder, the cylinder head and the bottom of the intake valve. The inflow boundary, the intake valve top, the intake valve and the intake port are defined as parts in region 1. The intake boundary condition is defined at the entry plane of the intake port. The pressure of the intake boundary is fixed. Since only the intake flow is studied, the exhaust port is not included in this model. The omission of the exhaust port can improve the rate of convergence to reduce the simulation time. The geometry details of this engine model are summarized in Table 1.

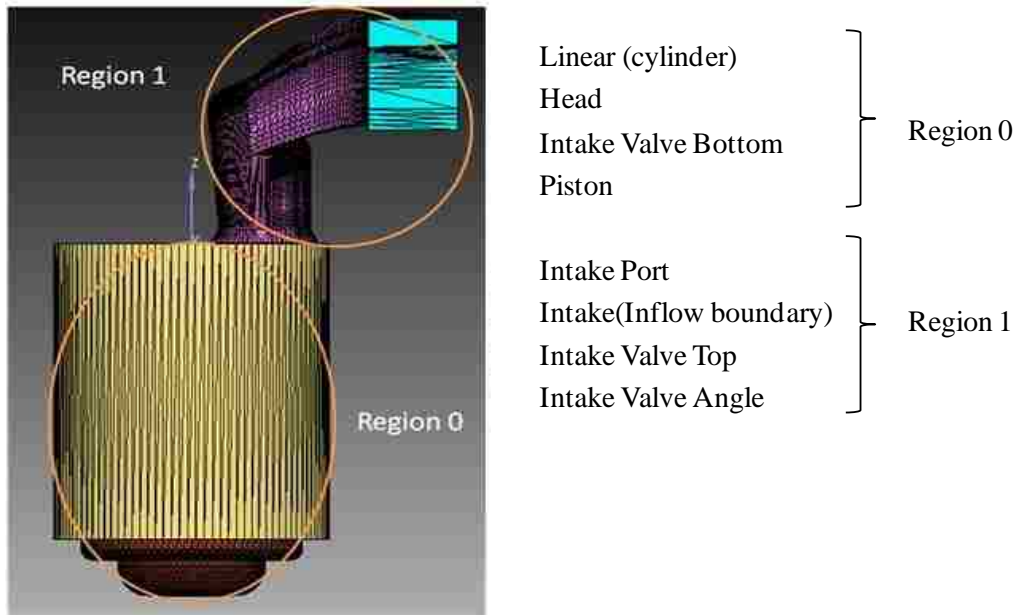


Figure 14 Boundary conditions and regions of Yanmar NFD-170 engine model

Table 1 Geometrical characteristics of Yanmar NFD-170 engine

<i>Property</i>	<i>Dimension</i>
Bore (m)	0.102
Stroke (m)	0.105
Squish (m)	0.002
Connect rod (m)	0.165
Compression ratio (-)	13.1:1

There are seven sets of boundary conditions in the steady state model, which are separated into three regions as shown in Figure 15. There is no piston in this model, and the outflow boundary is created to replace the piston and defined as region 2. The intake boundary condition is defined at the entry plane of the intake ports and the outlet boundary condition is specified at the cylinder exit plane. The steady state air flow calculations are performed with four different intake mass flow rates and constant pressure conditions are initially assigned at both the inlet and the cylinder. The static pressure is given at the bottom of the cylinder and walls are assumed as non-slip conditions.

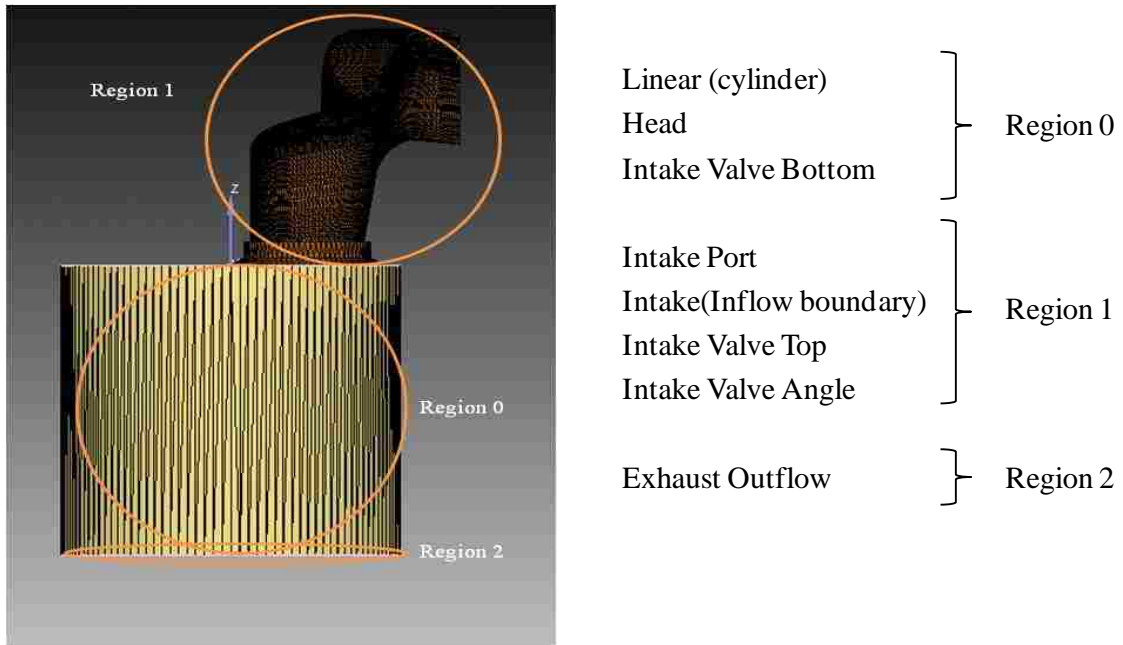


Figure 15 Boundary conditions and regions of the steady state model

The velocity distribution at the intake plane is designated as a uniform mean velocity profile based on the measured or specified flow rate. The outlet boundary conditions specified at the cylinder exit plane are that the flow at all locations in this plane would be directed outwards and that continuity is satisfied at the exit (Figure 16).

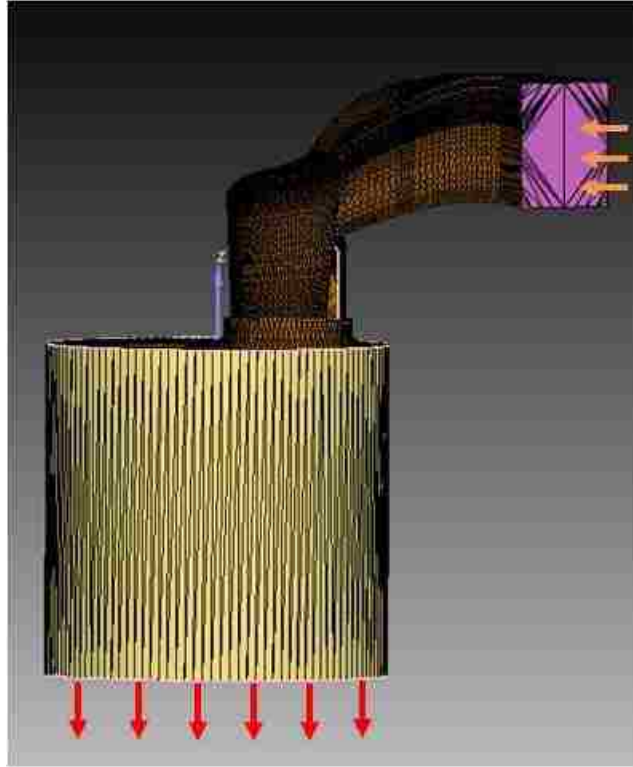


Figure 16 Inflow and outflow direction of the steady state model

2.2.3 Simulation conditions

The simulation conditions are set in the input files. The flows are simulated with a $k-\epsilon$ turbulence model and a “law of the wall” formulation, as defined by CONVERGE, is specified at all the solid surfaces. As mentioned before, different engine speeds are simulated using the transient Yanmar NFD-170 engine model and the steady state model is simulated under similar conditions with different mass flow rates, which are correlated to different engine speeds. The engine model simulations with different engine speeds are simulated first and the details of the simulation conditions are provided in Table 2. The average mass flow rate for each condition is calculated from the transient simulation results and these results are used as the initial mass flow rates of the steady state model simulations.

Table 2 Simulation conditions for the Yanmar NFD-170 engine model

<i>Engine speed (rpm)</i>	<i>Intake pressure (bar)</i>	<i>Intake temperature (K)</i>	<i>In cylinder pressure (bar)</i>
1250	1	298	1
1500	1	298	1
1750	1	298	1

The initial temperature of the engine cylinder is also set at 298K for all the cases. Since only the intake flow is investigated, the simulation starts at 360°CA before the compression TDC and ends at 120°CA before the compression TDC. The simulation conditions for the steady state model are listed in Table 3. Instead of using the engine speed, the intake mass flow rate correlated to the engine speed is used. These simulations are run under the steady state. Normally, the first order upwinding is used for the numerical scheme, when running a steady state simulation. This is because the first order upwinding method adds the numerical viscosity which tends to aid in the convergence [8].

Table 3 Simulation conditions for the steady state model

<i>Mass flow rate (g/s)</i>	<i>Intake pressure (bar)</i>	<i>Intake temperature (K)</i>	<i>In cylinder pressure (bar)</i>
\dot{m}_{1250}	1	298	1
\dot{m}_{1500}	1	298	1
\dot{m}_{1750}	1	298	1

2.3 Calculation and post-processing

There are two types of output files generated from a simulation in CONVERGE: spatially averaged data and the cell-by-cell data [8]. Each line of the data in the cell averaged output files represents the values of one particular cycle or time-step. In the cell-by-cell files, the calculated results for each individual cell in the domain are provided – one file for each time step at the user-specified frequency.

The CONVERGE package does not have a way of visualizing the output directly [8]. Instead, it has a converter to allow the output to be converted into formats for visualization in either EnSight or GMV. The converter can also create cell-by-cell output files in column format for the variables selected.

In this work, the output files are converted to the cell-by-cell output in column format and the Matlab is used as a tool to visualize the simulation results. The Matlab code is provided in appendix B.

CHAPTER 3

EMPIRICAL SETUP AND OPERATING CONDITIONS

3.1 Empirical setup

The geometry of the intake port and the cylinder head are shown in Figure 17. The present work is performed based on a Yanmar NFD-170 diesel engine model, which has a cylinder bore of 102 mm and a stroke of 105 mm. The velocity components, U , V , W are defined in the co-ordinate directions x , y and z respectively.

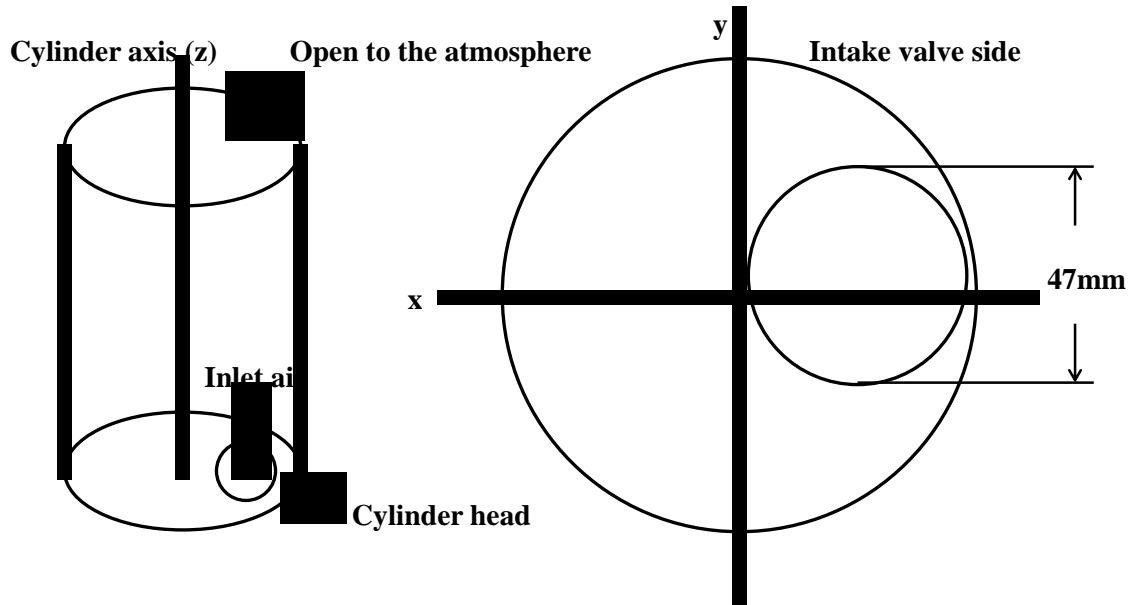


Figure 17 Geometry of the cylinder and the Yanmar NFD-170 cylinder head

The experiments are conducted under steady flow conditions using a helical intake port and the cylinder head of the Yanmar NFD-170 diesel engine. Air is employed as the working fluid. In this experimental setup a steady flow of air passes through the cylinder head with a fixed intake valve position into an open-ended transparent cylinder. A flow meter and a pressure gauge are used to measure the air flow rate and intake air pressure.

When the air flows through the intake port, it mixes with water droplets, about 3 μm in size. This mixture then goes into the cylinder to allow optical access of laser beams for the LDA measurements. Measurements are obtained with a valve lift of 6 mm. The physical setup of this experiment is shown in Figure 18. Figure 19 provides the schematic representation of the experiment setup.

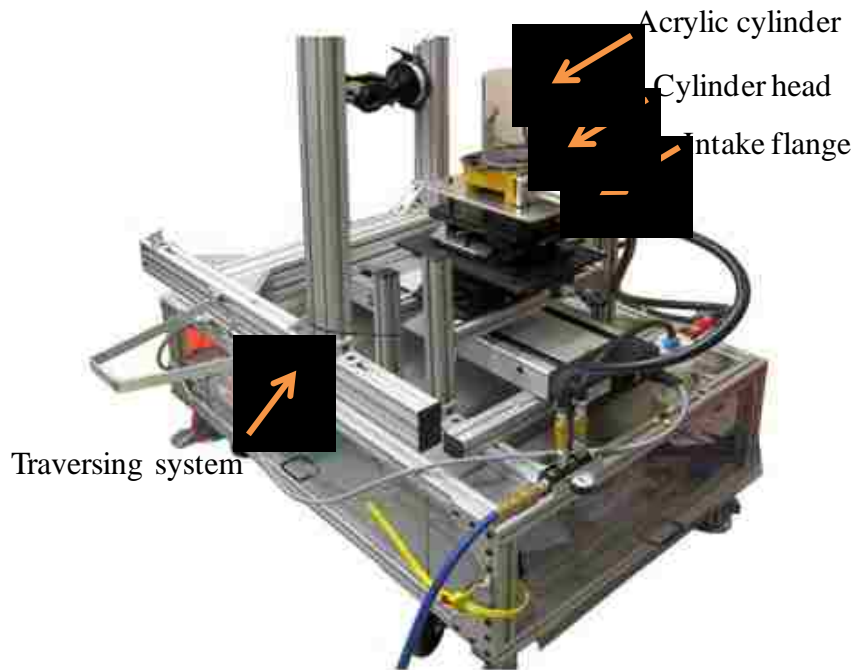


Figure 18 Experiment setup

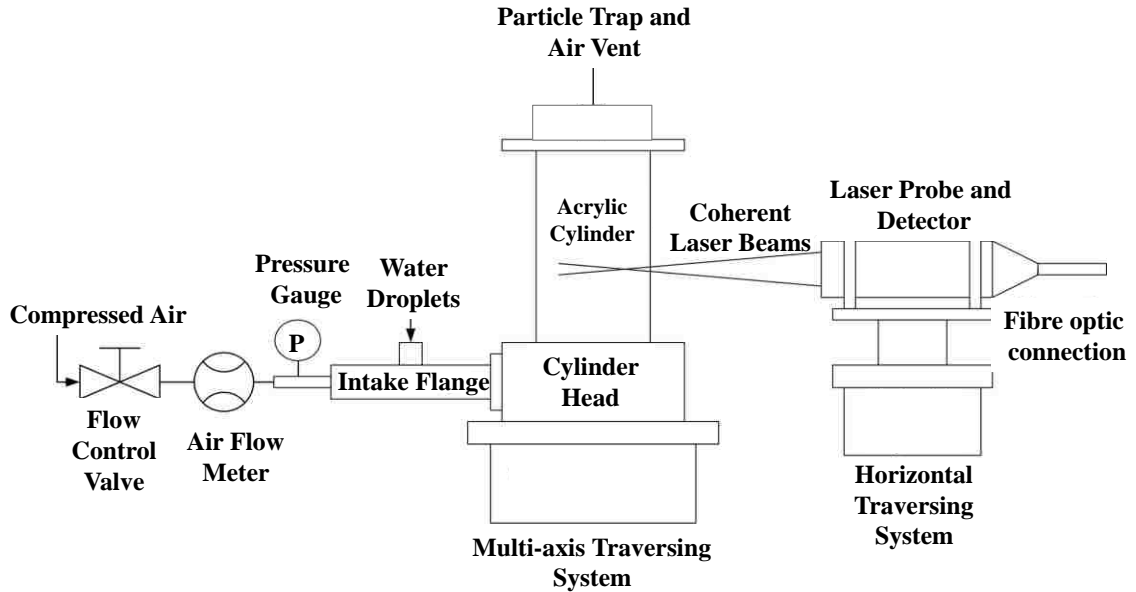


Figure 19 Schematic diagram of the experiment setup

The laser Doppler anemometer is operated in the backward-scatter fringe mode. The anemometer comprises of a 5W argon gas laser to provide a continuous beam for the Doppler anemometry, which is shown in Figure 20. The power of each coherent beam is approximately 50mW. The laser probe and the detector unit are coupled to the Dantec Dynamics Fiberflow system to perform point-by-point measurements of the velocity of the in-cylinder air flow, which is shown in Figure 21. The measurement volume is 4.08 mm long x 0.19 mm wide.



Figure 20 5W argon gas laser

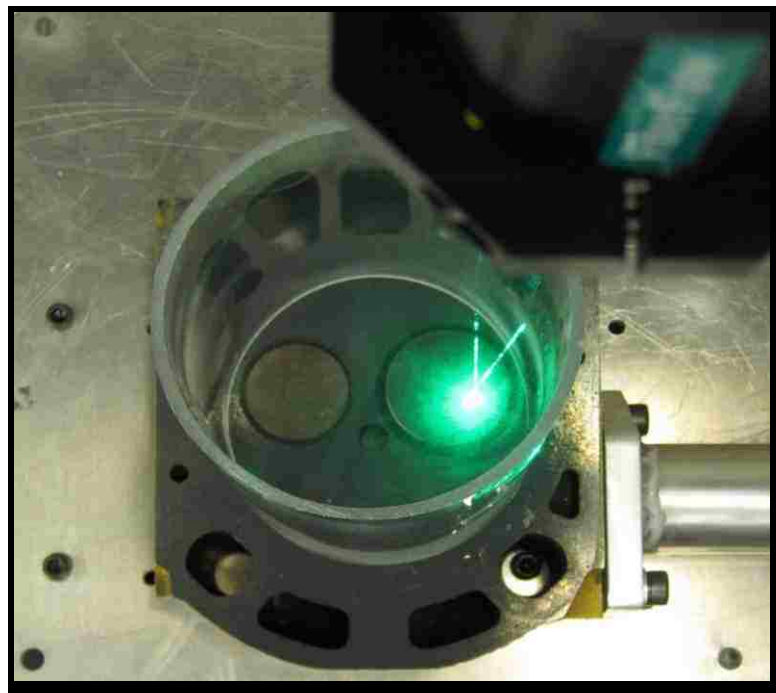


Figure 21 Point-by-point velocity measurement

The accuracy of the velocity field determination is ultimately limited by the ability of the seeding particles to follow the actual flow continuously. A proper tracer must be small enough to follow the fluid motion and should not influence the flow properties. On the other hand, the tracer needs to have a sufficient volume to scatter sufficient light. It is

also critical to have a uniform distribution of seeding particles in the measuring area to obtain a complete flow field. After an analysis of seeding materials and generation methods, fine water droplets are found to be a suitable seeding material for the present in-cylinder air motion investigation. Five water nebulizers are connected to the cylinder intake port to generate enough water droplets for the experiments. The size of the water droplet is approximately 3 μm diameter. The compressed air is passed into the cylinder with the water droplets to obtain a proper flow field that can be measured by the laser system. In order to reduce the reflection of the laser beams from the transparent cylinder during the laser measurement, half of the cylinder is covered by a piece of black paper.

3.2 Operating conditions

As mentioned in Chapter 1, an engine in-cylinder air flow is usually studied under transient conditions with a piston. However, in this thesis, the intake flows without a piston under steady state conditions are presented. Due to the limitation of the experiment setup, the maximum mass flow rate of air is 2.5 g/s. The number of seeding particles drops significantly at higher air flow rates, resulting in difficulties obtaining the laser scattering. Currently, only the case with 2.5 g/s mass flow rate is measured. Table 4 lists the steady state experiment conditions.

Table 4 Experiment condition

<i>Mass flow rate (g/s)</i>	<i>Outflow pressure (bar)</i>	<i>Intake temperature (K)</i>	<i>In-cylinder pressure (bar)</i>
2.5	1	298	1

CHAPTER 4

RESULTS AND DISCUSSION

4.1 Transient Yanmar NFD-170 engine model simulation results

The Yanmar NFD-170 engine model is simulated at four different engine speeds, 1000 rpm, 1250 rpm, 1500 rpm and 1750 rpm to estimate the in-flow conditions. The mass flow rates are calculated by the simulation software at 0.1°CA resolutions. The direction of the mass flow is normal to the inflow/outflow boundary plane. A positive value indicates the flow direction out of the domain while a negative value indicates the flow direction into the domain [8]. From Figure 22 the mass flow rates are negative during the intake valve open period, which means the air flows in through the intake port. The average mass flow rate is calculated, between points a and b, by the following formula for each engine speed,

$$\dot{m} = \frac{\sum_a^b \dot{m}_{i+1} (t_{i+1} - t_i)}{t_b - t_a} \quad (7)$$

Where,

a is the zero-crossing point representing the start of the intake flow

b is the zero-crossing point representing the end of the intake flow

The calculated average mass flow rate values of each engine speed are shown both in Table 5 and in Figure 24.

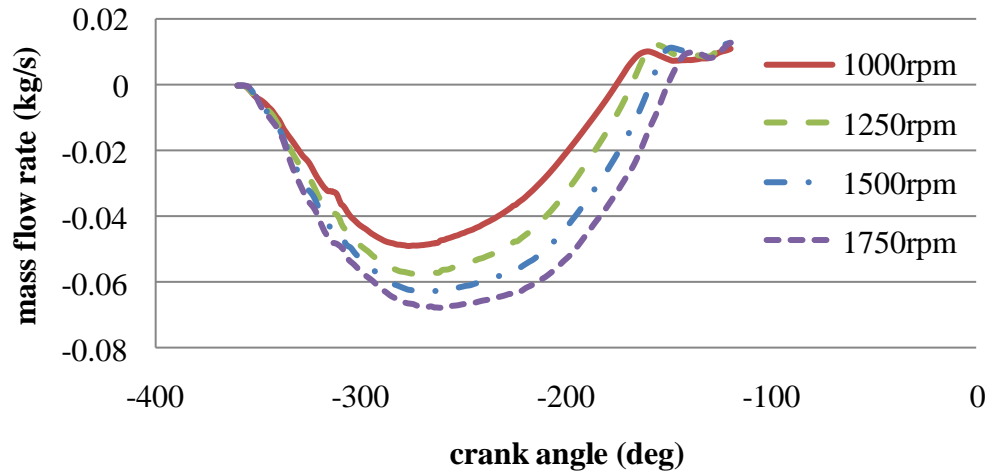


Figure 22 Mass flow rate vs. crank angle

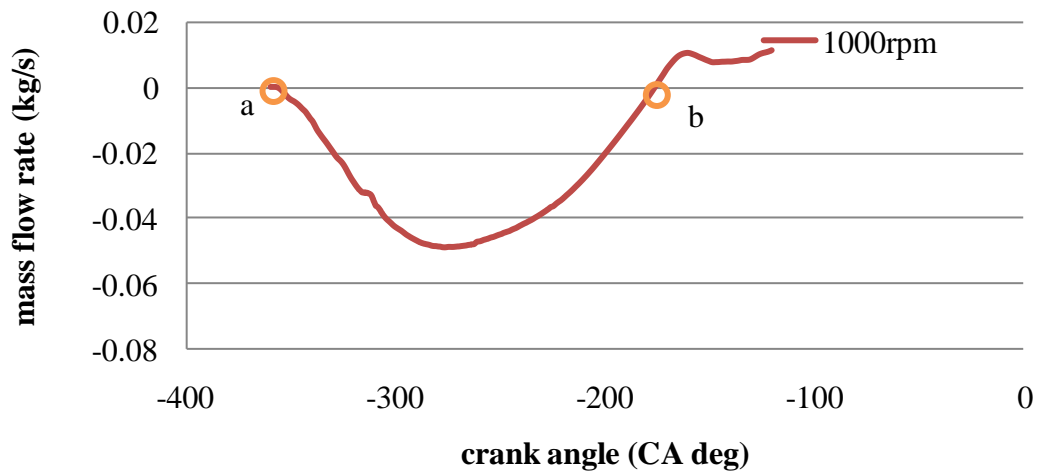


Figure 23 Average mass flow rate calculation

Table 5 Average mass flow rate of different engine speeds

<i>Engine speed (rpm)</i>	<i>Average flow rate (g/s)</i>
1750	45.23
1500	41.54
1250	36.51
1000	30.37

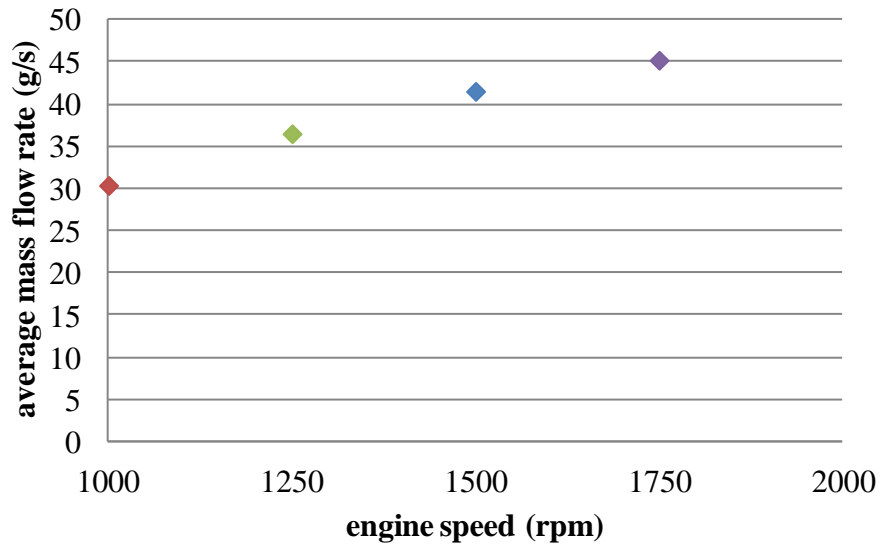


Figure 24 Average mass flow rate vs. engine speed

4.2 Steady state model simulation results

From the calculation concluded above, the initial mass flow rates of the experiment model simulations are set to be 45 g/s, 41.5 g/s and 36.5 g/s, respectively. As mentioned in Section 2.2.1, the steady state solver uses simulation ‘cycles’ in the input file, instead of ‘time’. In order to have a better understanding of the simulation process, the simulation cycles are converted to time based on the total mass flow into the intake port and the mass flow rate for that specified cycles (equation 8). The equivalent time duration for 2000 cycles is about 20 ms for those three mass flow rates. The intake mass flow rate is kept constant during the whole simulation process.

To visualize the output, Matlab codes (Appendix B) are written to plot the air flow field from the simulation output files. Quiver plots and contour plots are created.

$$t = \frac{m_{total}}{\dot{m}} \quad (8)$$

The CFD results show that the mean RMS velocities are scaled with the intake mass flow rates. Figure 25 shows the relation between the mean RMS velocity and the running time at different mass flow rates. The in-cylinder mean RMS velocity is increasing as the air flows into the cylinder. At higher mass flow rates, the mean RMS velocity increases, representing an increased turbulent motion of the intake flow. The turbulence kinetic energy at equivalent engine speeds is shown in Figure 26. Turbulence kinetic energy is calculated based on the mean RMS velocity; and the relation between TKE and mean RMS velocity is given in equation 9.

$$k = \frac{3}{2} u^2 \quad (9)$$

From the formula above, higher velocity flows carry higher kinetic energy, which can be observed in Figure 26.

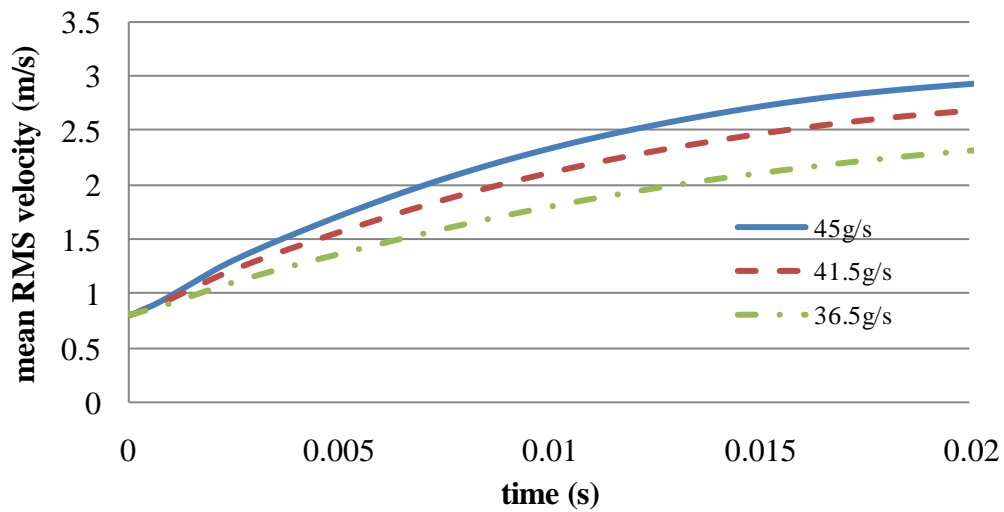


Figure 25 Mean RMS velocity at different mass flow rates

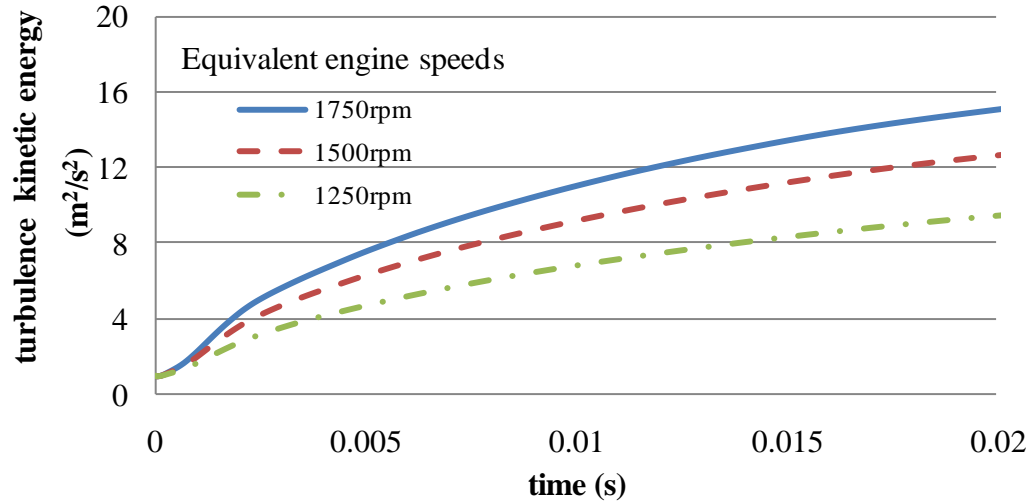


Figure 26 Turbulence kinetic energy at equivalent engine speeds

The in-cylinder flow structures at both vertical and horizontal planes are analyzed for these three conditions. The center plane of the intake cylinder named XZ plane, is selected as the vertical plane in this study and the middle plane of the cylinder (50mm from the top of the cylinder head), called XY plane, is selected as the horizontal plane. The positions of the XZ plane and the XY plane are shown in Figure 27. It is noted that the boundary layer velocity has not been calculated for any of the simulation cases.



Figure 27 Positions of the selected analysis planes

In the first case, the air is introduced through the intake port at a flow rate of 45 g/s and the resulting flow structure in XZ plane is presented in Figure 28. The quiver plot displaces the velocity vectors as arrows with components (u, v, w) at the point (x, y, z). The size of the quiver indicates the relative velocity value at each point. The velocity for all cells at the inflow/outflow surface is calculated from [8].

$$u_i = \frac{\dot{m}}{\rho_{ave} A} n_i \quad (10)$$

where,

\dot{m} is the mass flow rate

ρ_{ave} is the average density at the boundary surface

A is the total area of the inflow/outflow surface

n_i is the outward pointing surface normal

From the equation shown above, the mean velocity of air at the intake surface is about 25.5 m/s. There is a recirculation region presenting at 10 mm from the cylinder head surface. The air in the recirculation zone recombines with the flow along the cylinder wall. The flow on the left along the wall represents the flow introduced into this plane from the intake port and the flow from other planes. The central region of this plane shows a large tumble-like vortice with velocities ranging from 5 m/s to 20 m/s. The magnitude of the velocity in this plane is shown in Figure 29 and the position of the intake valve is also indicated for reference. A high velocity flow is created through the valve and along the cylinder head; with the highest velocity in an order of 50 m/s.

In the XY plane a symmetrical flow structure is created about the center plane of the intake valve, at $y=10$ mm. The flow structure in XY plane for this case is shown in Figure 30. Several swirling vortices are present in this horizontal plane and two main rotating vortices, one clockwise and the other one counter-clockwise, are observed on each side of the $y=10$ mm plane. At the center of the cylinder, the air travels towards right. The highest velocity is approximately 35 m/s as shown in Figure 31 and the relatively high velocities are observed near the wall. The region beneath the intake valve has a low magnitude of horizontal velocity, as shown on the right of Figure 31, which indicates that the flow is moving mainly downwards.

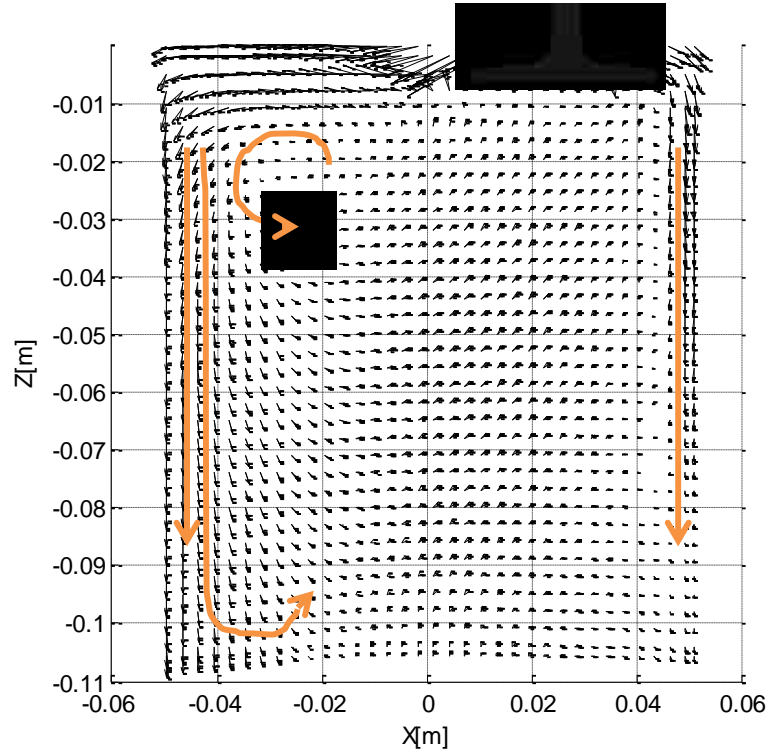


Figure 28 Velocity vectors in XZ plane with mass flow rate of 45 g/s

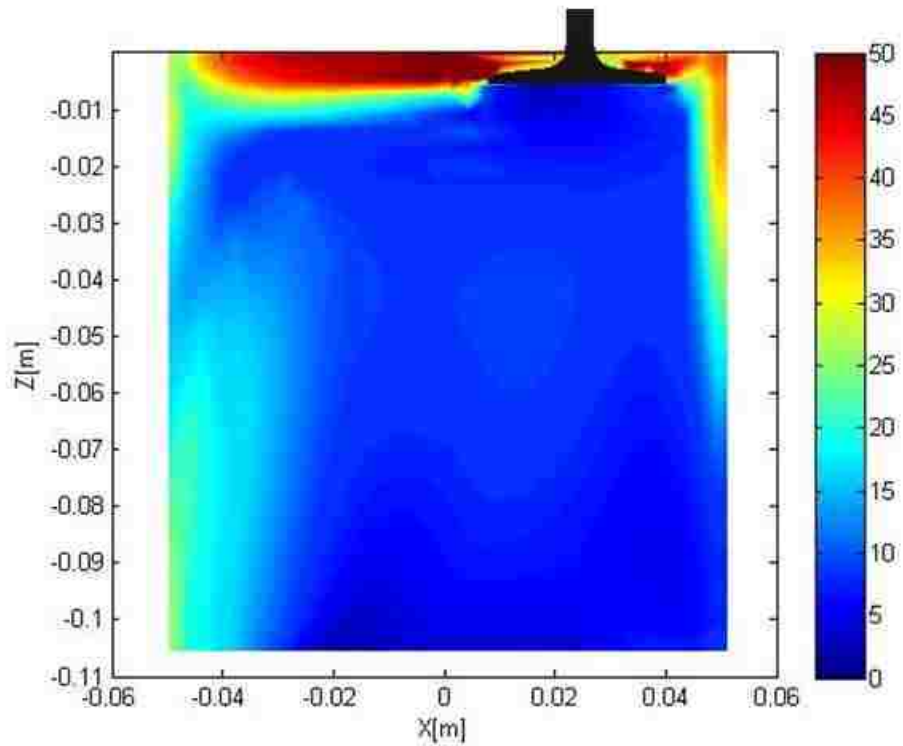


Figure 29 Magnitude velocity in XZ plane with mass flow rate of 45 g/s

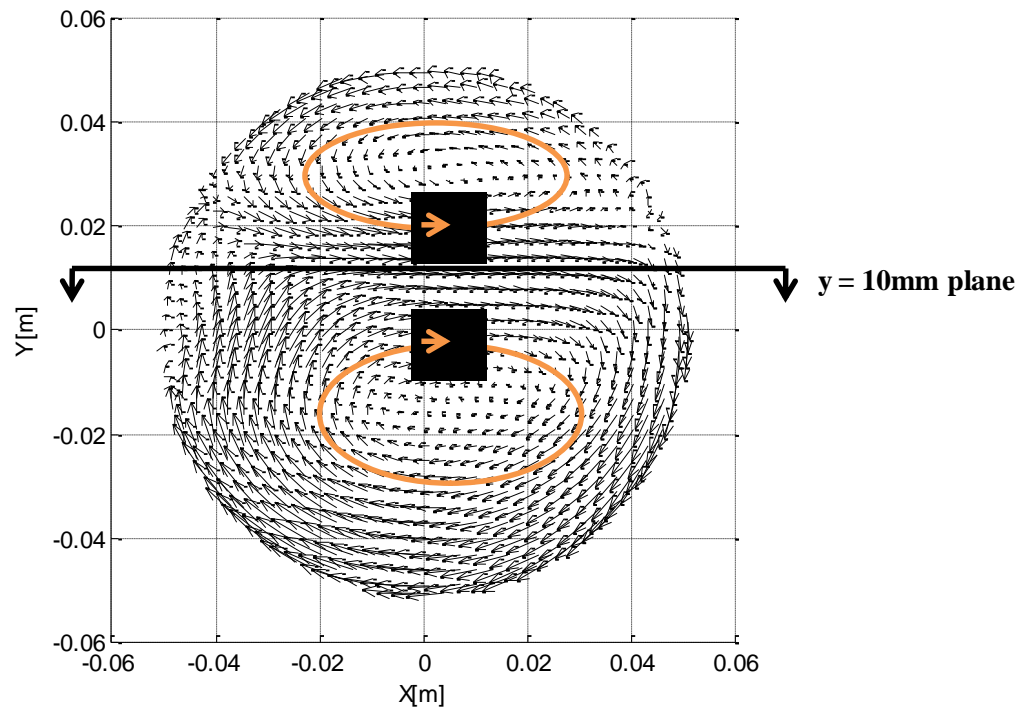


Figure 30 Velocity vectors in XY plane with mass flow rate of 45 g/s

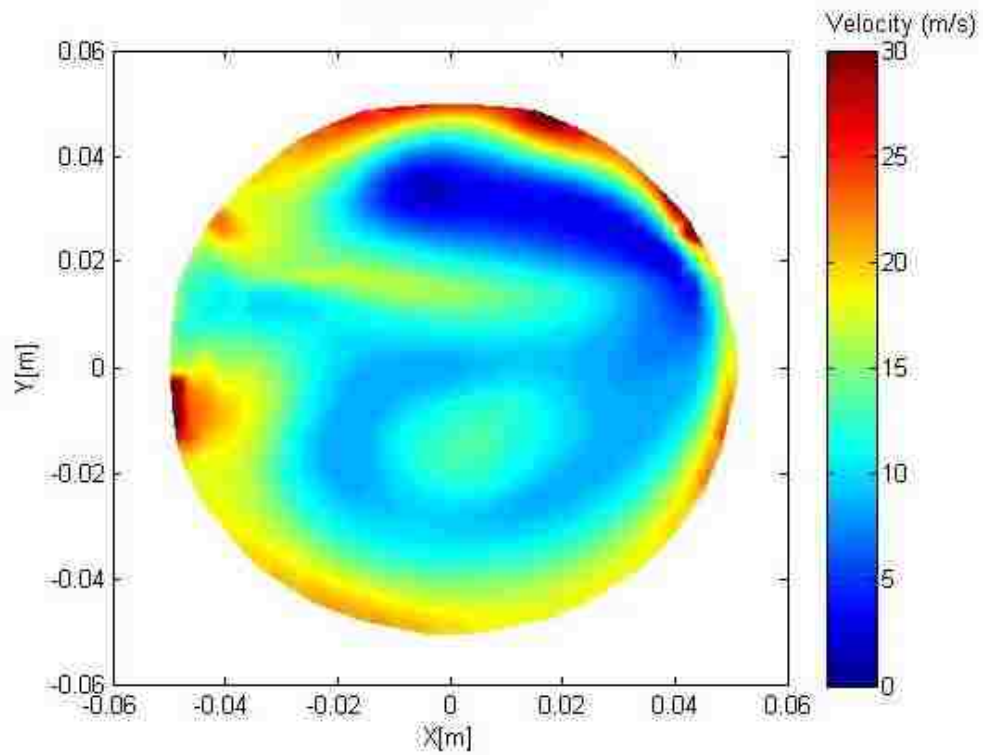


Figure 31 Magnitude velocity in XY plane with mass flow rate of 45 g/s

When the mass flow rate decreases from 45 g/s to 41.5 g/s while maintaining an intake valve lift of 6 mm, the mean air velocity decreases to 23.9 m/s. Figure 32 shows the velocity vectors in the XZ plane. The flow field and the velocity magnitudes (Figure 33) are very similar to the simulation results with the mass flow rate of 45 g/s. However, the lower mass flow rate results in a reduced high-velocity region.

The velocity vectors for the mass flow rate of 41.5 g/s in XY plane are shown in Figure 34. This flow structure includes two rotating vortices, one clockwise and the other one is counter-clockwise, which is similar to Figure 30. The magnitude of the velocity in this horizontal plane is shown in Figure 35. Comparing with Figure 31, the velocity near the wall with the mass flow rate of 41.5 g/s is lower than that in the 45 g/s case.

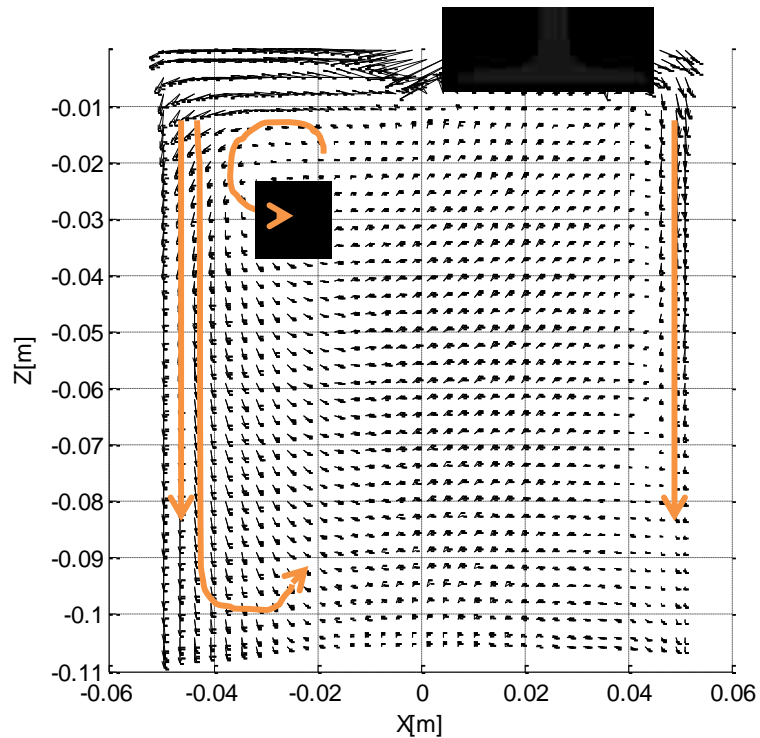


Figure 32 Velocity vectors in XZ plane with mass flow rate of 41.5 g/s

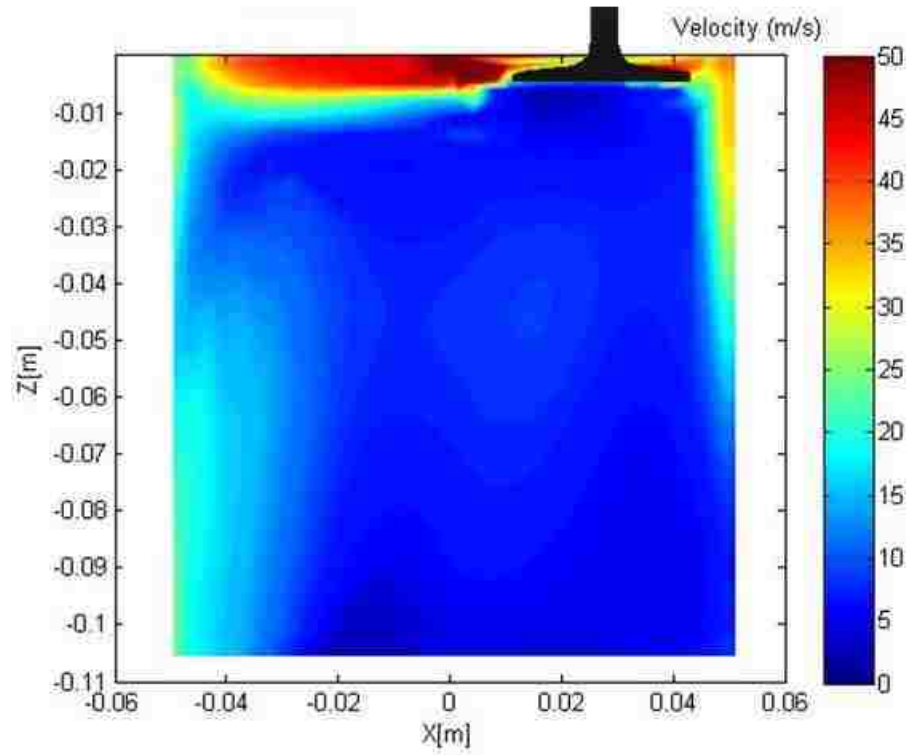


Figure 33 Magnitude velocity in XZ plane with mass flow rate of 41.5 g/s

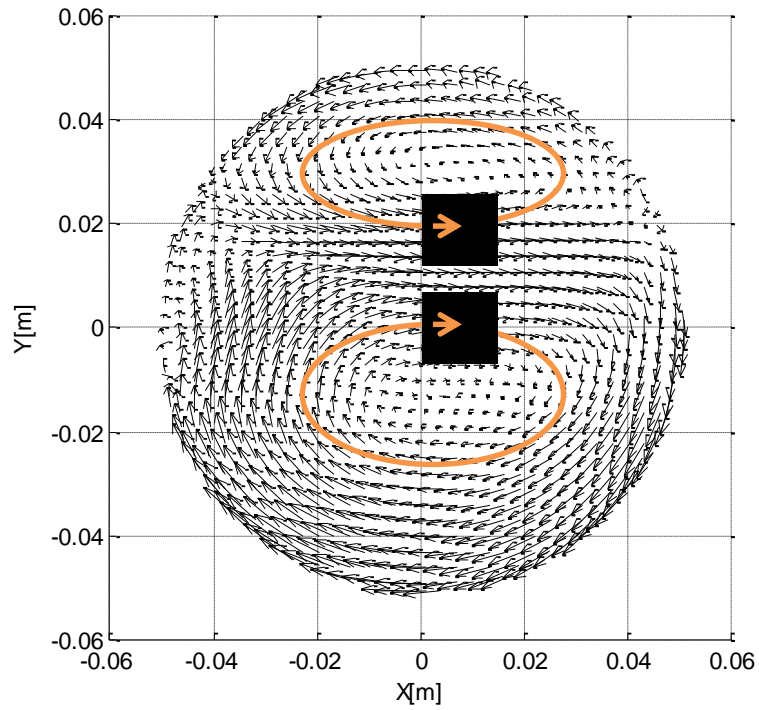


Figure 34 Velocity vectors in XY plane with mass flow rate of 41.5 g/s

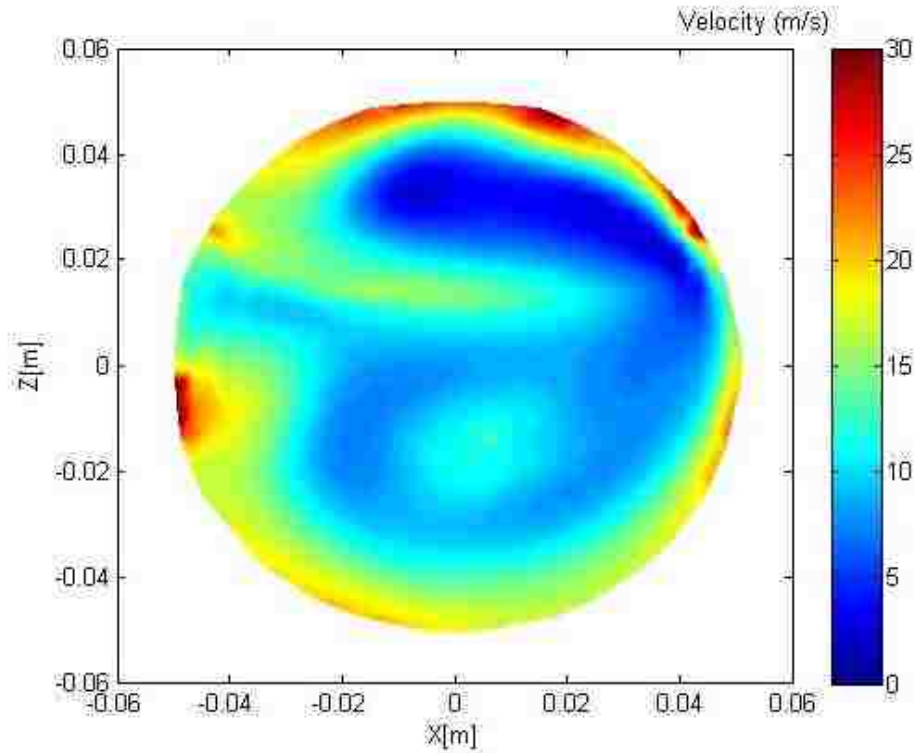


Figure 35 Magnitude velocity in XY plane with mass flow rate of 41.5 g/s

For the case equivalent to 1250 rpm engine speed, the mass flow rate reduces to 36.5 g/s with the intake valve lift maintained at 6 mm. The average intake air velocity decreases by about 10% compared to the second case, from 23.9 m/s to 21.5 m/s. Velocity vectors in XZ plane are shown in Figure 36. Qualitatively, the flow patterns are similar to those with mass flow rates of 45 g/s and 41.5 g/s, but differences are observed that the area with higher velocities (Figure 37) is smaller than those in the previous two cases.

Figure 38 shows the in-cylinder flow field in the XY plane. As expected, the flow direction in this plane is the same as the first case. Vortices are observed at each side of the $y=10$ mm plane and they merge at the central part of the cylinder in this plane. The flow moves towards the cylinder wall. The magnitude of velocity is shown in Figure 39. The velocity magnitude remains the same, 0 to 30 m/s. The highest velocity calculated in

this plane is about 27 m/s. The air flow near the cylinder wall also has lower velocities than those in the 45 g/s and 41.5 g/s conditions cases.

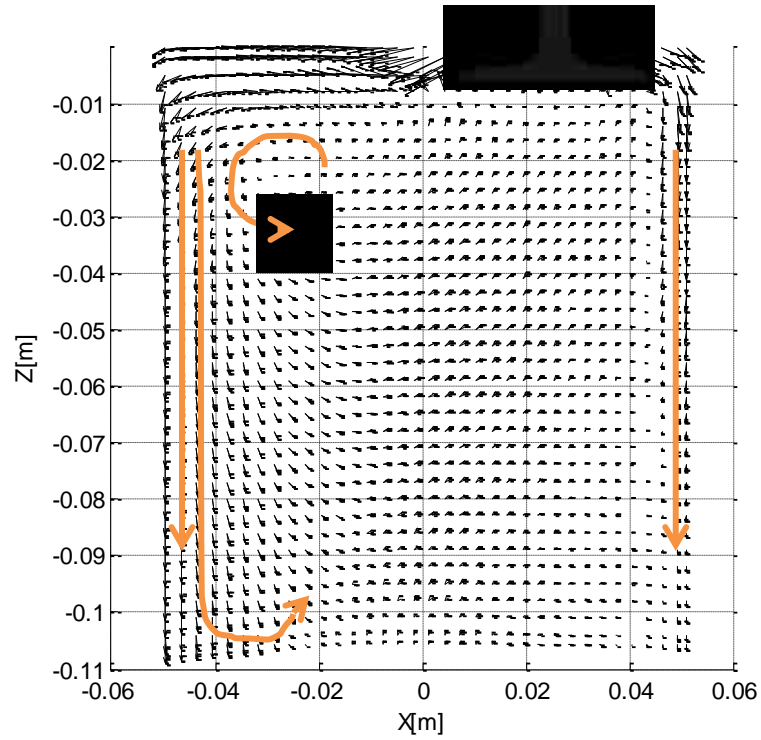


Figure 36 Velocity vectors in XZ plane with mass flow rate of 36.5 g/s

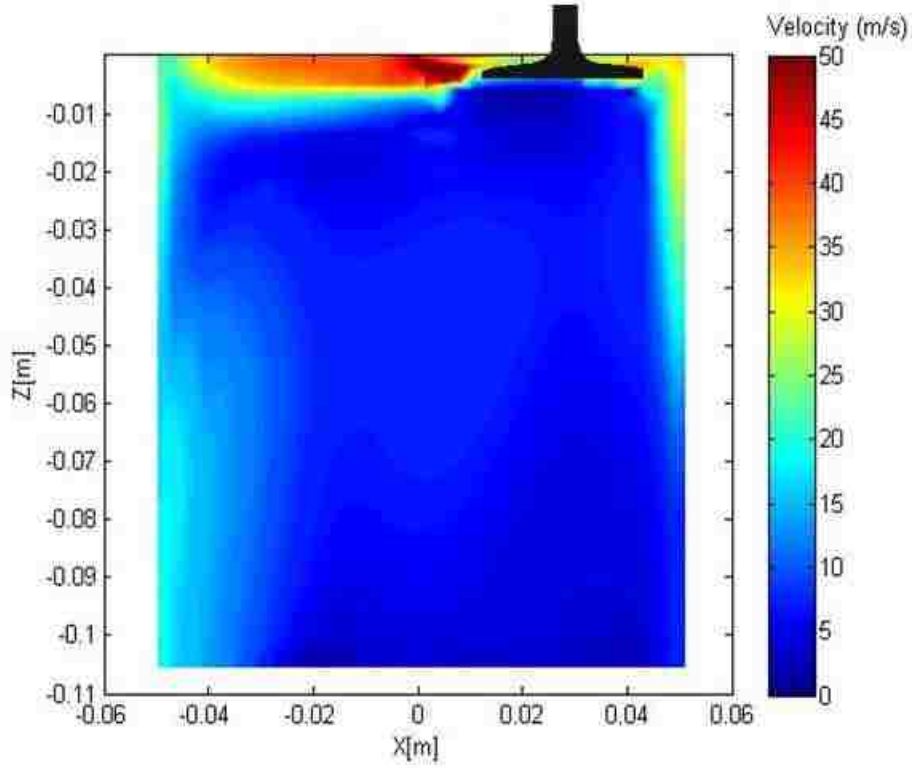


Figure 37 Magnitude velocity in XZ plane with mass flow rate of 36.5 g/s

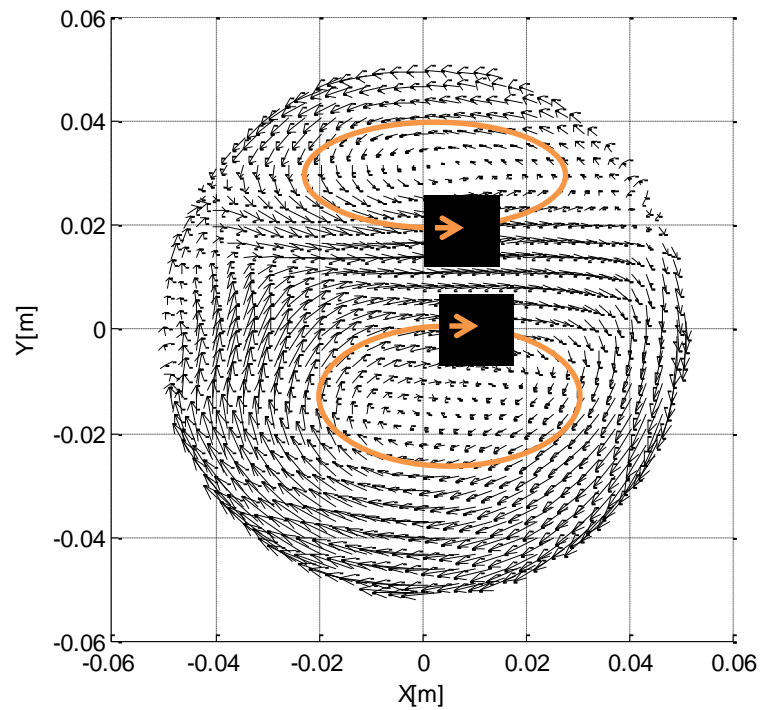


Figure 38 Velocity vectors in XY plane with mass flow rate of 36.5 g/s

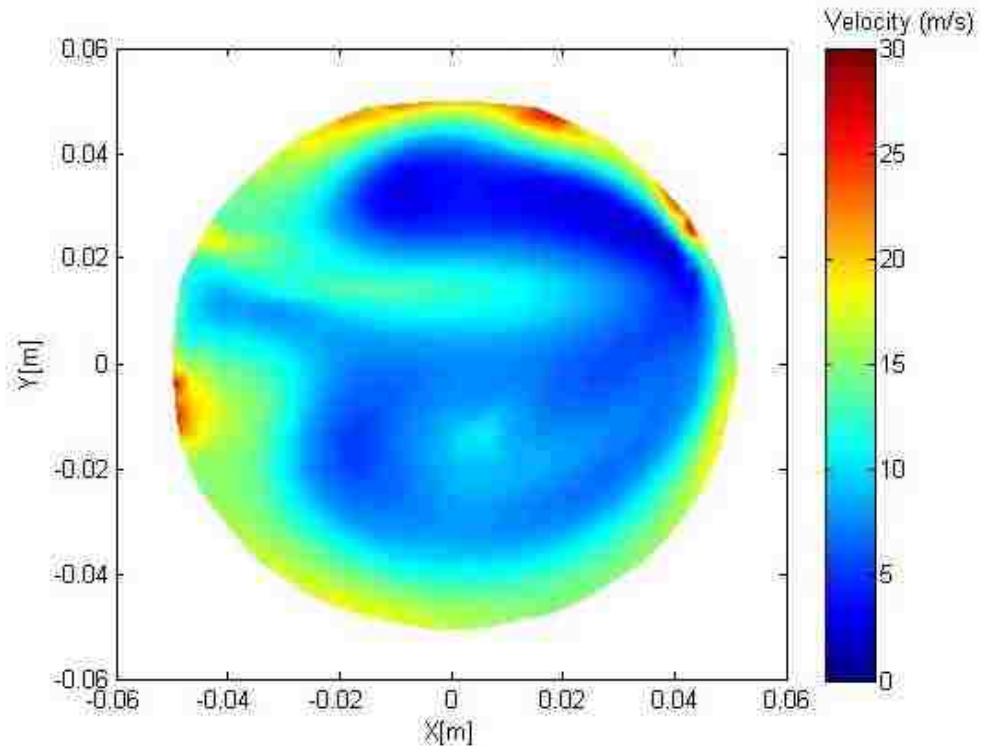


Figure 39 Magnitude velocity in XY plane with mass flow rate of 36.5 g/s

Table 6 summarizes the influence of the mass flow rate on the average intake air velocity. The average intake air velocity is increased in a similar way to the mass flow rates.

Table 6 Increments on mass flow rates and average intake air velocity

<i>Mass flow rate</i> (g/s)	<i>Average intake air velocity</i> (m/s)	<i>Percentage increase (%)</i>	
		<i>Mass flow rate</i>	<i>Average velocity</i>
36.5	21.5	-	-
41.5	23.9	13.7	11.2
45	25.5	23.3	18.6

In order to develop deeper understanding of the effect of the mass flow rates on the flow structures, a case with the mass flow rate of 4 g/s is simulated. Velocity vectors in the XZ plane and in XY plane are presented in Figure 39 and Figure 41. Although the mass flow rate reduces by 10 times compared with the highest mass flow rate in previous simulations (45 g/s), the flow pattern in the same vertical and horizontal planes are still very similar to other cases. However, the magnitude of velocities shown in Figure 40 and

Figure 42 indicate that the highest velocity decreases significantly. For the XZ plane, the highest velocity is still shown near the intake valve. However, compared to the results of the 45 g/s case, the magnitude of the highest velocity decreases from 50 m/s to 6 m/s. For the XY plane, the magnitude velocities are lower than 3.5 m/s with a flow rate of 4 g/s, while the highest magnitude velocity can reach up to 30 m/s with an intake mass flow rate of 45 g/s.

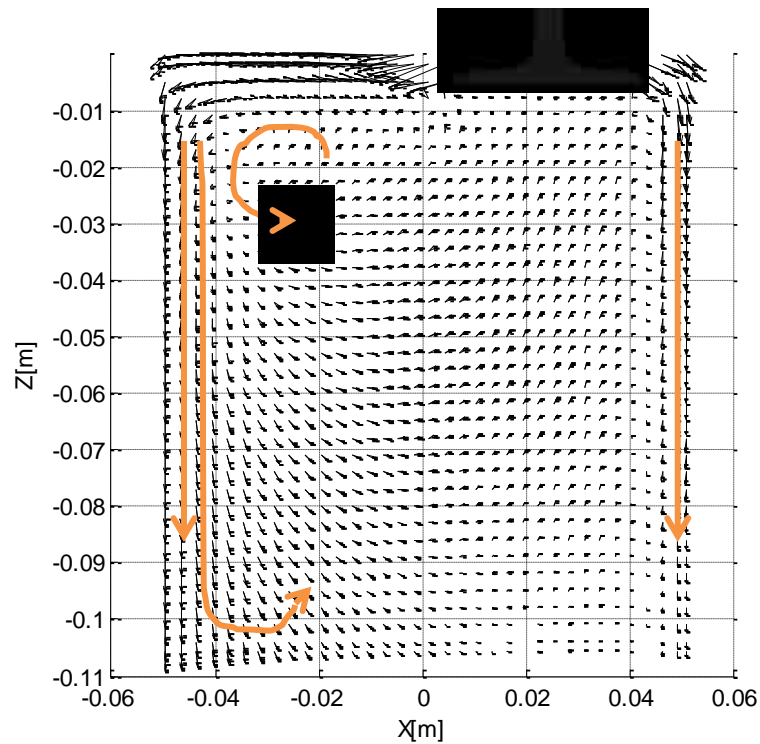


Figure 40 Velocity vectors in XZ plane with mass flow rate of 4 g/s

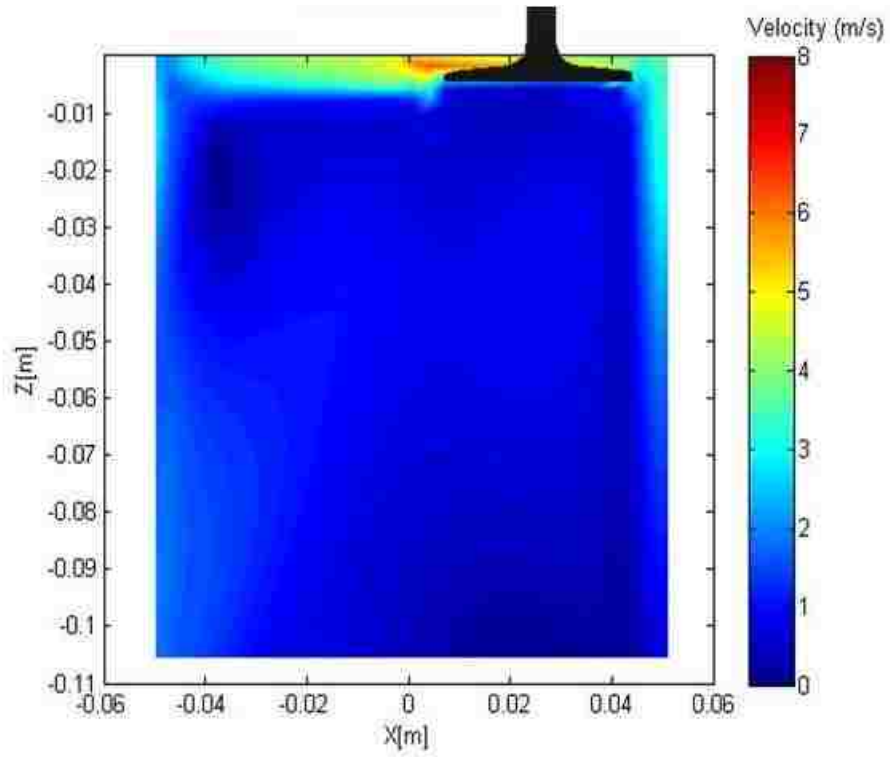


Figure 41 Magnitude velocity in XZ plane with mass flow rate of 4 g/s

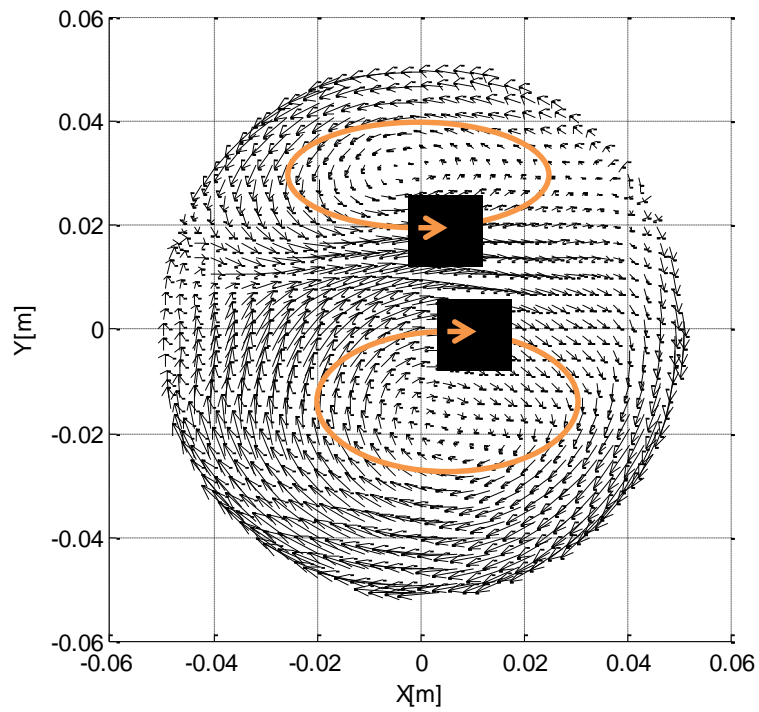


Figure 42 Velocity vectors in XY plane with mass flow rate of 4 g/s

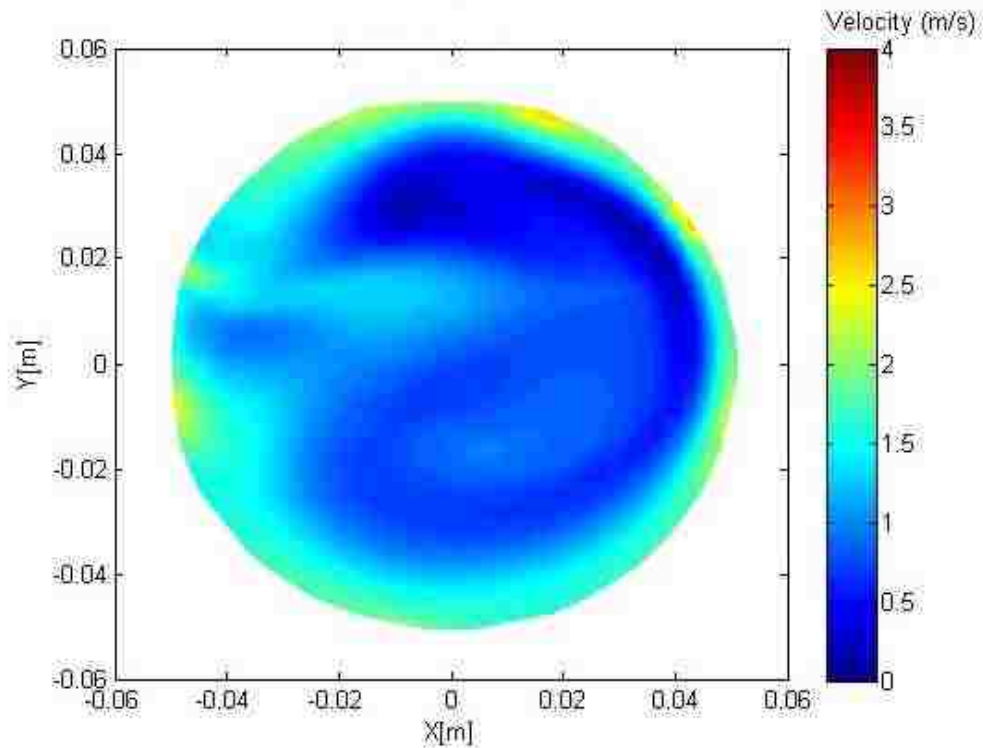


Figure 43 Magnitude velocity in XY plane with mass flow rate of 4 g/s

From the results and discussion above, the flow patterns do not change much as the mass flow rate changes while maintaining the intake valve lift at 6 mm. The mean RMS velocities and magnitude velocities are scaled with mass flow rates. This indicates the mass flow rate seems to have minor effects over the in-cylinder flow patterns, even though the flow in the cylinder is very complex. As expected, the values of magnitude velocities change. These results confirm similar findings reported by other researchers [14].

4.3 Steady state experimental results

Experiments are concluded using the LDA technique. Since the laser system cannot measure the magnitude velocity at a specific point directly, three velocity components, u , v , w , are measured at x , y , z direction respectively. The magnitude velocities are calculated by using the following formula:

$$V_{mag} = \sqrt{u^2 + v^2 + w^2} \quad (11)$$

where,

u is the velocity component at x axis

v is the velocity component at y axis

w is the velocity component at z axis

Velocity vectors of three XY planes and one XZ plane are measured with the laser system. Table 7 provides the parameters of the measured planes. The first XY plane is selected at 2 mm above the intake valve plane and the intake valve lift is kept at 6 mm for all the experiments. The position of the second XY plane is selected at 19 mm above the valve, which is about quarter of the length of the cylinder. The plane at half length of the cylinder is selected as the third XY plane, which is 50 mm above the cylinder head. The measurement grid of these three planes is 4 mm x 4 mm, 8 mm x 8 mm and 8 mm x 8 mm, respectively. The central vertical XZ plane of the cylinder is chosen to measure the velocity vectors. The height of this plane is 62 mm in z axis from the bottom of the cylinder. The 4 mm x 4 mm grid is used in this plane. The positions of these three XY planes are shown in Figure 44 and Figure 45 shows the position of the XZ plane.

Table 7 Property of measured planes

<i>XY plane</i>		
<i>Plane #</i>	<i>Plane position relative to the valve plane (mm)</i>	<i>Measured grid (mm x mm)</i>
1	2	4 x 4
2	19	8 x 8
3	44	8 x 8
<i>XZ plane</i>		
<i>Plane #</i>	<i>Plane position</i>	<i>Measured grid (mm x mm)</i>
4	The central XZ plane of the cylinder	4 x 4

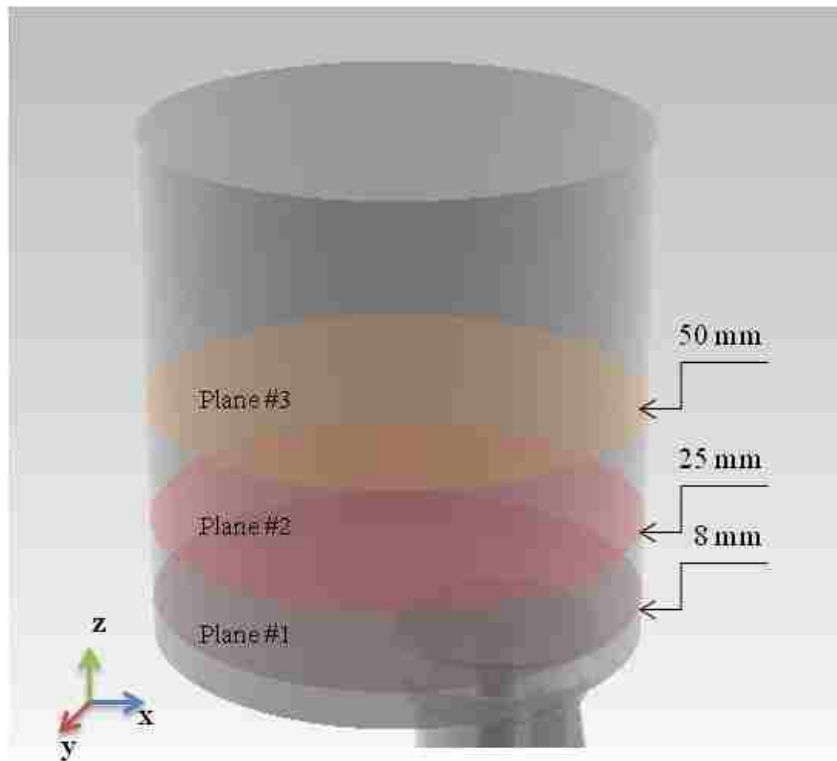


Figure 44 Positions of selected XY planes

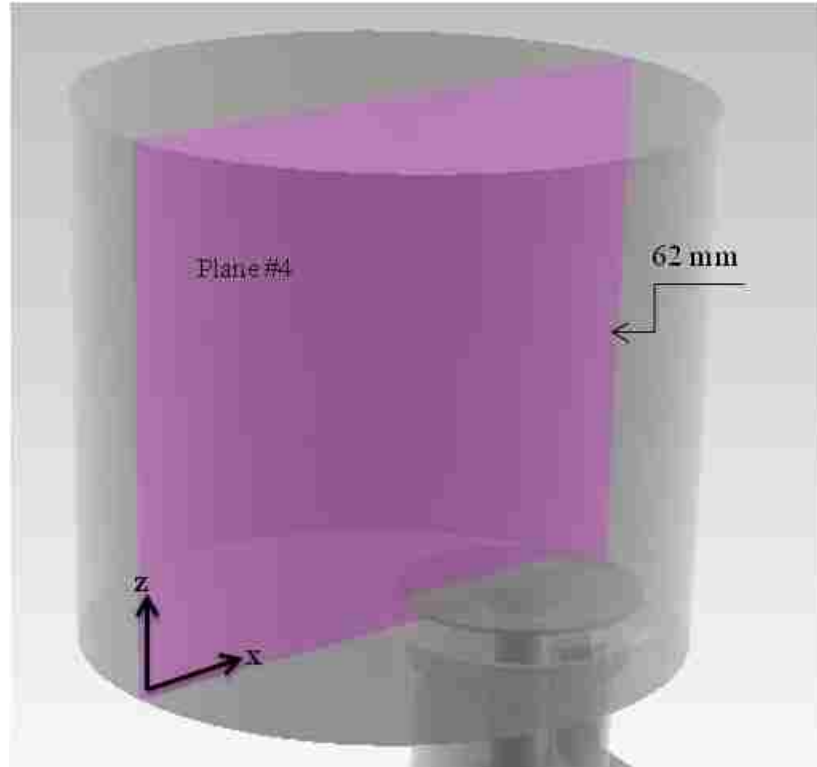


Figure 45 Position of selected XZ plane

The maximum mass flow rate under current experiment circumstance is about 2.5 g/s, which is much lower than the average mass flow rate of the reference engine at 1750 rpm. In order to better understand the meaning of this mass flow rate, the equivalent engine speed of this mass flow rate is calculated based on previous simulation results. As shown in Figure 46, the relationship between average mass flow rate and engine speed is approximately linear. The value of equivalent engine speed at 2.5 g/s is about 176 rpm from the calculation shown in Figure 46.

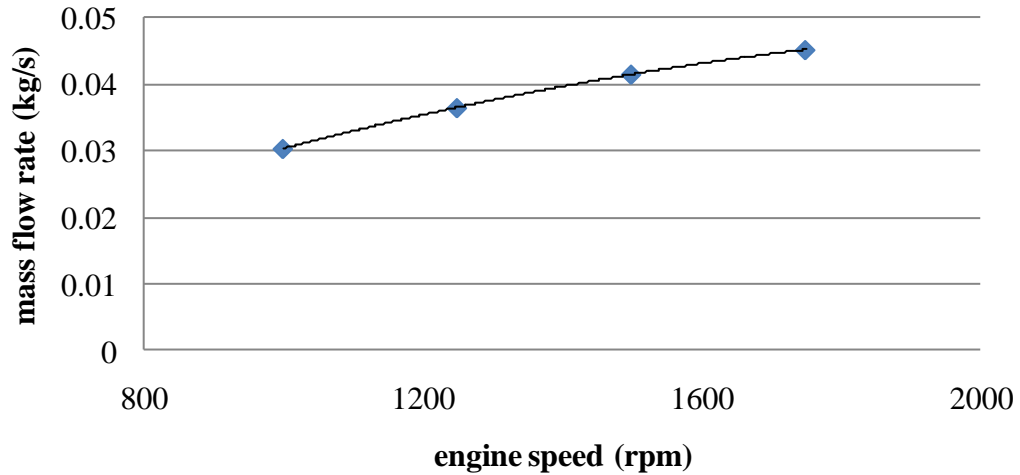


Figure 46 Average mass flow rate at different engine speeds

The measured velocity vectors in $z=8$ mm plane at a valve lift of 6 mm are presented in Figure 47. The air flows into the cylinder through the intake valve towards the cylinder wall. Because this plane is very close to the intake valve, the region beneath the intake valve can be seen clearly, which is shown on the right side of Figure 47. The smaller horizontal velocity vectors indicate that the air is mainly flowing upwards.

The LDA results in $z=25$ mm plane are shown in Figure 48. The air flow generated in this plane has two circular regions on either side of the $y=0$ mm plane. At the center of this plane, the flow travels towards the intake valve to the right.

The measured results in the $z=50$ mm plane are presented in Figure 49. The flow field in this plane has similar structure compared with that in the $z=25$ mm plane, but there are differences. From the figure, it is observed that the centers of the two circular regions are closer to the intake valve.

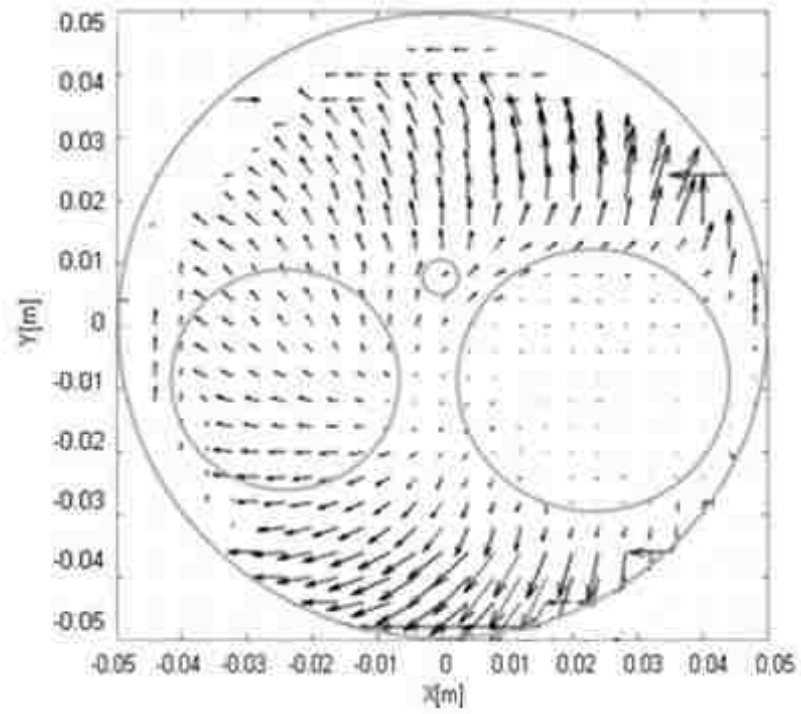


Figure 47 Velocity vectors in $z=8$ mm plane

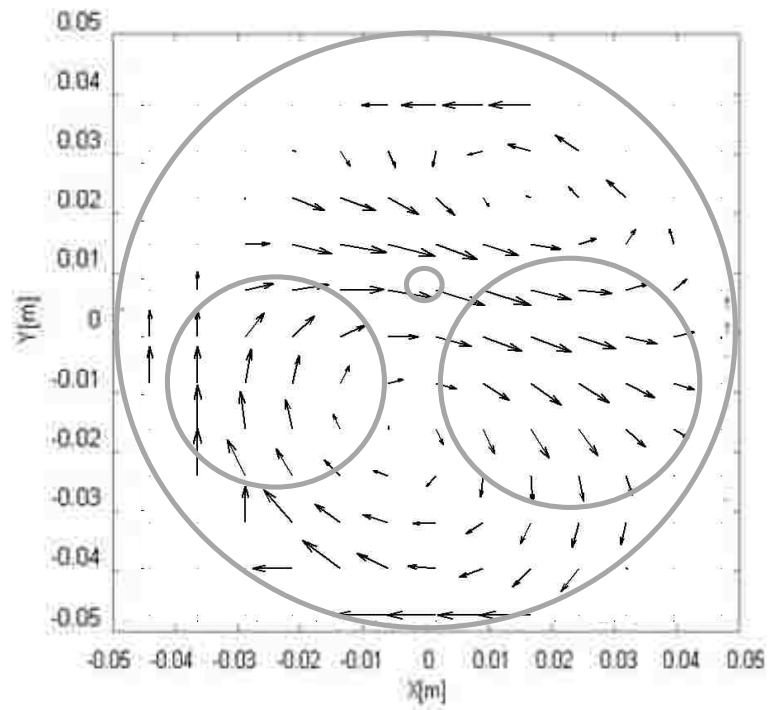


Figure 48 Velocity vectors in $z=25$ mm plane

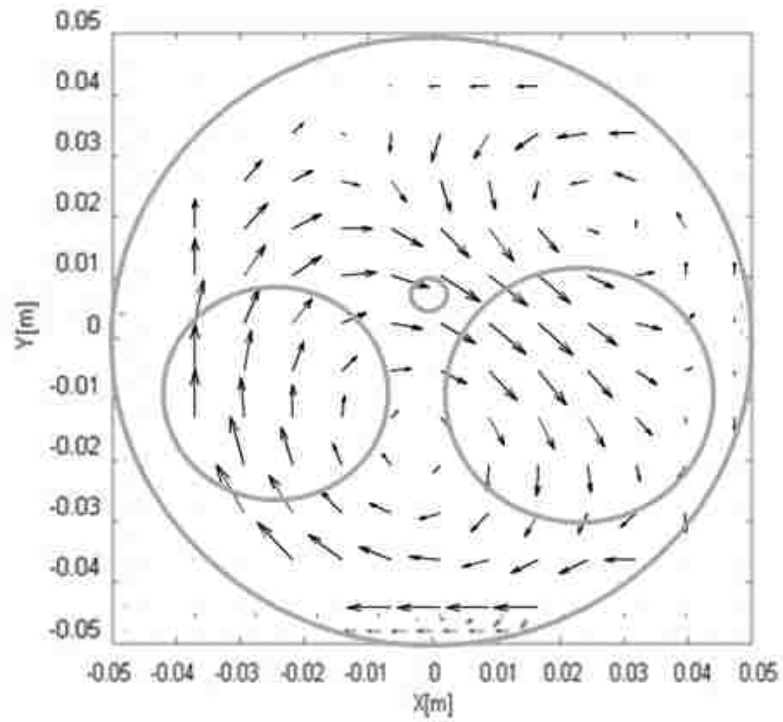


Figure 49 Velocity vectors in $z=50$ mm plane

Figure 50 shows the LDA measured results of the flow field in the XZ plane. A circular shaped vortice is produced by the air passing to the left of the intake valve. The direction of the flow near the cylinder boundary is along the cylinder wall. There are some tumble-like structures in the center area of this plane.

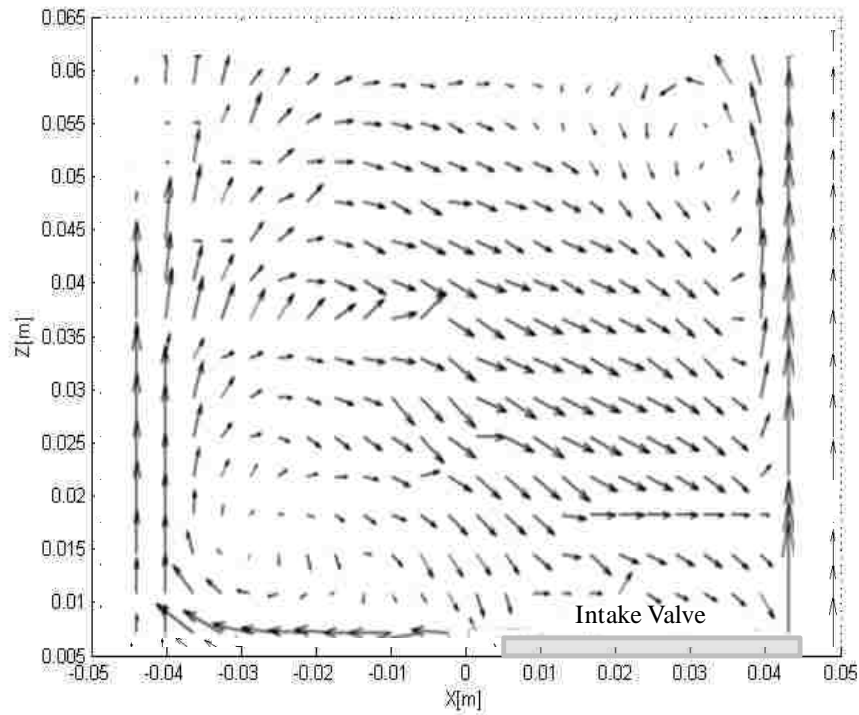


Figure 50 Velocity vectors in the center XZ plane of the cylinder

4.4 Comparison of model predictions and measurements

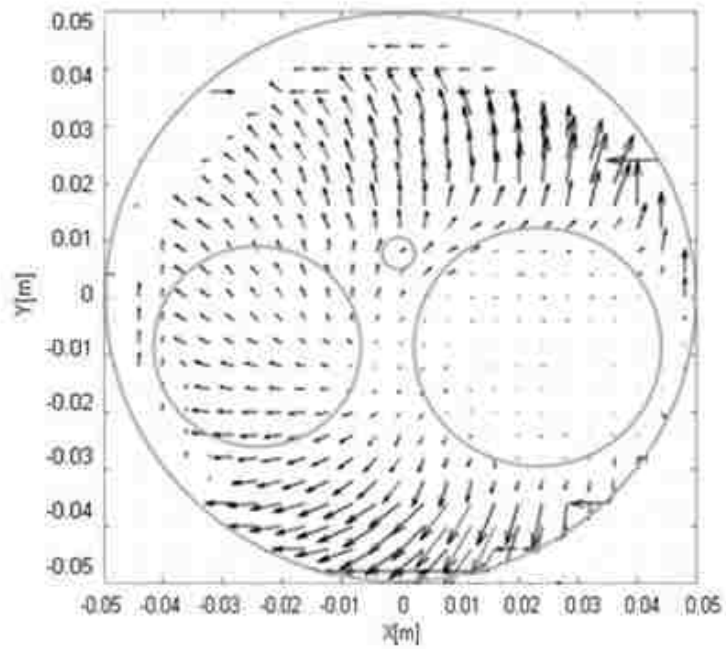
The flow structures with the intake mass flow rate of 2.5 g/s at different planes are simulated in the CONVERGE package. The simulation conditions are set according to the experiments. Figure 51 to Figure 53 compare the experiment and the simulation results of the flow field at different horizontal planes. The relative positions of major engine components including the exhaust valve, the injector, the intake valve and the engine bore are indicated by the grey circles in the figure. Figure 54 describes the measured and computed results of the flow field at the selected vertical plane. The measured empirical results are provided at the top part of each figure and the figure at the bottom part shows the simulation results.

Figure 51 compares the measured and computed velocity vectors in the $z=8$ mm plane at a valve lift of 6 mm. The air flow radiates outward from the valve in all directions. When the flow hits the cylinder wall, it travels along circumference at a high speed as expected. In most regions, the LDA and CFD results show good agreement in the flow directions. The simulation results give a more detailed description of the motion in each plane.

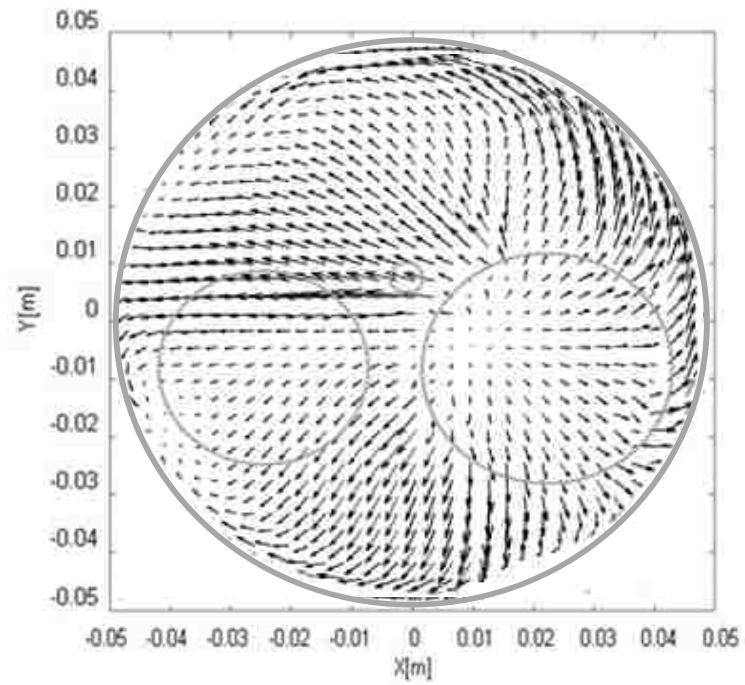
Figure 52 compares the measured and computed velocity vectors in the $z=25$ mm plane at a valve lift of 6 mm. In most regions, the LDA and CFD results show good agreement in the flow directions, even though the rotating centers of the two circular regions are more to the right in the simulation results than those in the measurement results.

The comparison of CFD and LDA velocity vector results in the $z=50$ mm plane is shown in Figure 53. There are some disagreements between the simulation and the measured results, especially, the two circular regions, which are not very clear in the simulation. The area close to the cylinder wall has better matching than the central part.

A comparison between CFD and LDA results in the central XZ plane of the cylinder are shown in Figure 54. A well match of the numerical and the experimental velocity vector results in this vertical plane is achieved. Both sets of results showed the structure of the air flow near the cylinder wall and the rotating vortices to the left of the intake valve.

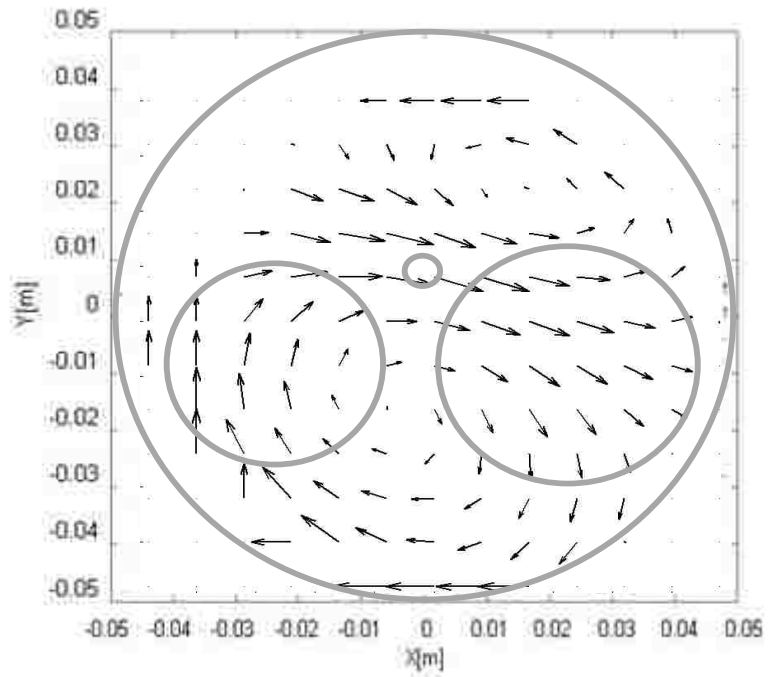


(a) Experiment results (plane # 1)

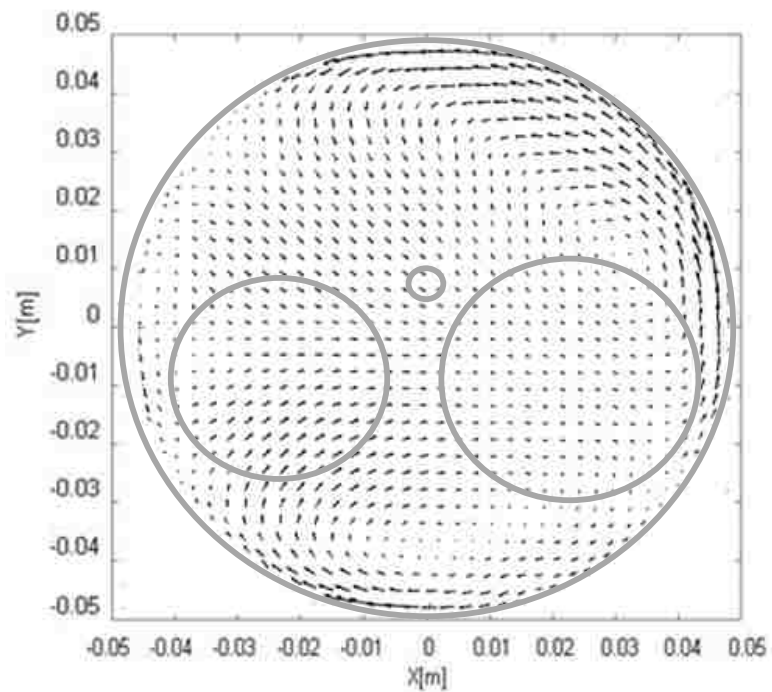


(b) Simulation results (plane #1)

Figure 51 Comparison of measured and computed velocity vectors in $z=8$ mm plane

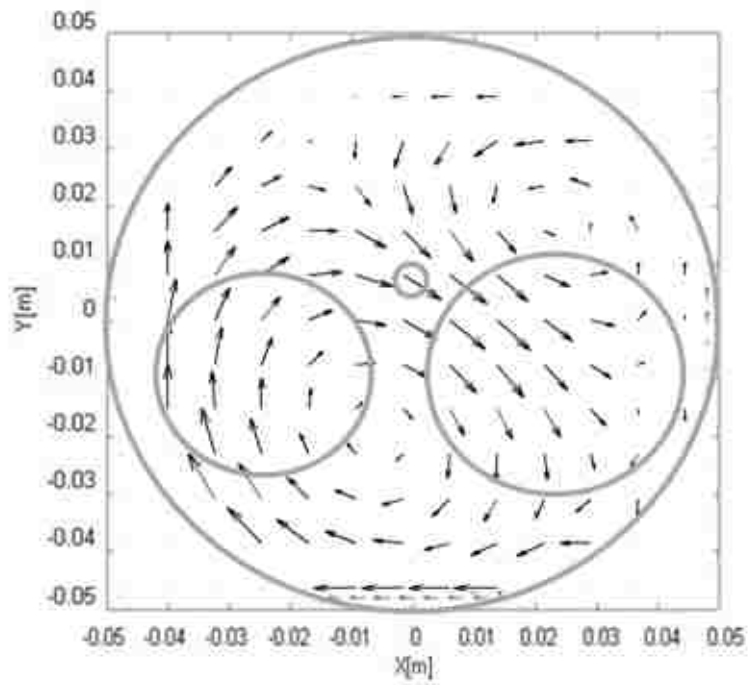


(a) Experiment results (plane # 2)

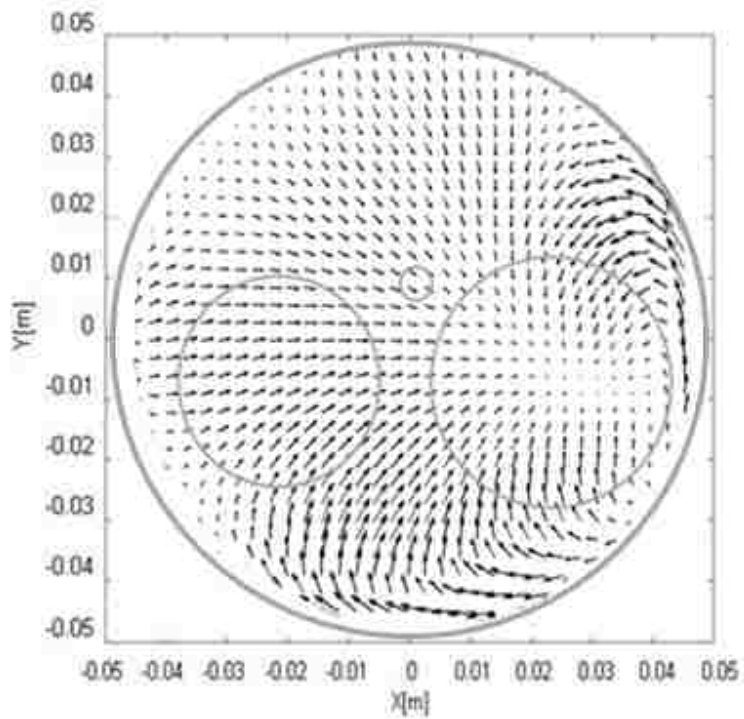


(b) Simulation results (plane #2)

Figure 52 Comparison of measured and computed velocity vectors in $z=25$ mm plane

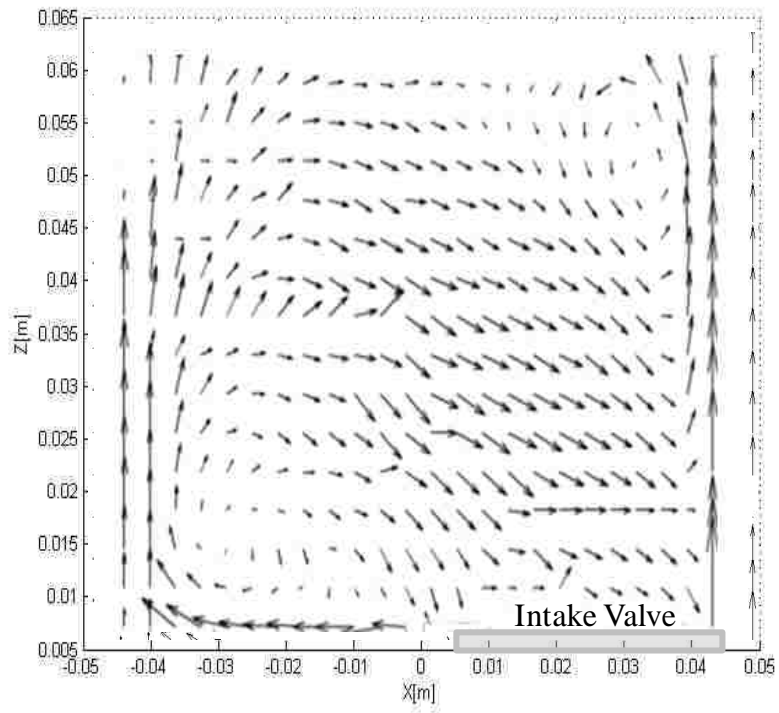


(a) Experiment results (plane # 3)

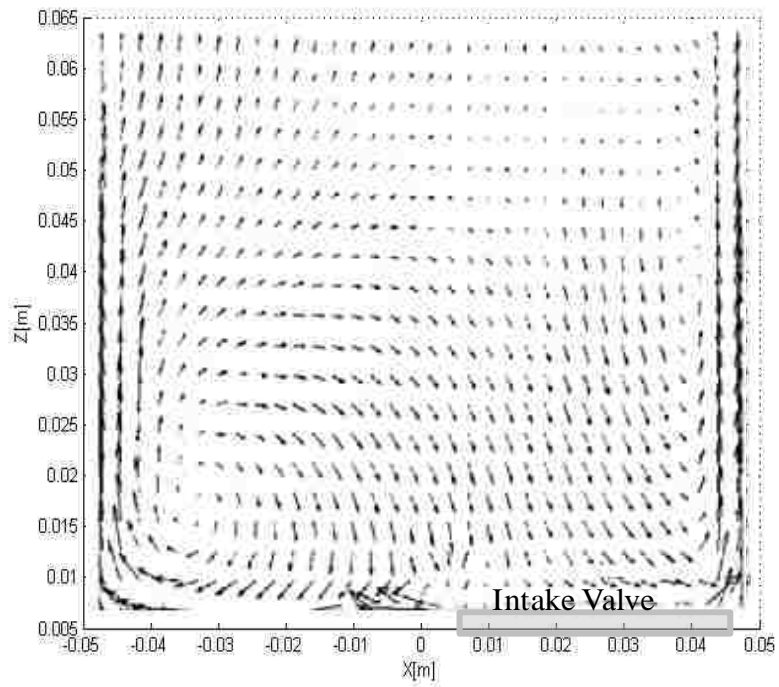


(b) Simulation results (plane #3)

Figure 53 Comparison of measured and computed velocity vectors in $z=50$ mm plane



(a) Experiment results (plane # 4)



(b) Simulation results (plane #4)

Figure 54 Comparison of measured and computed velocity vectors in the XZ plane

4.5 Limitations of steady state flow

The steady state flow setup has the ability to produce flow data which is closely but not entirely related to the actual engine performance. There are a few reasons that contribute to the inconsistency. First, the steady state flow tests have a steady pressure difference while in actual engines, the pressure differences are varied during the whole process. Figure 55 shows how the intake port pressures vary under transient flow conditions and during a steady flow test. This figure is obtained from the CONVERGE simulations. The mass flow rate of the air flow into the cylinder may change at different pressure differentials owing to the changes in Reynolds number.

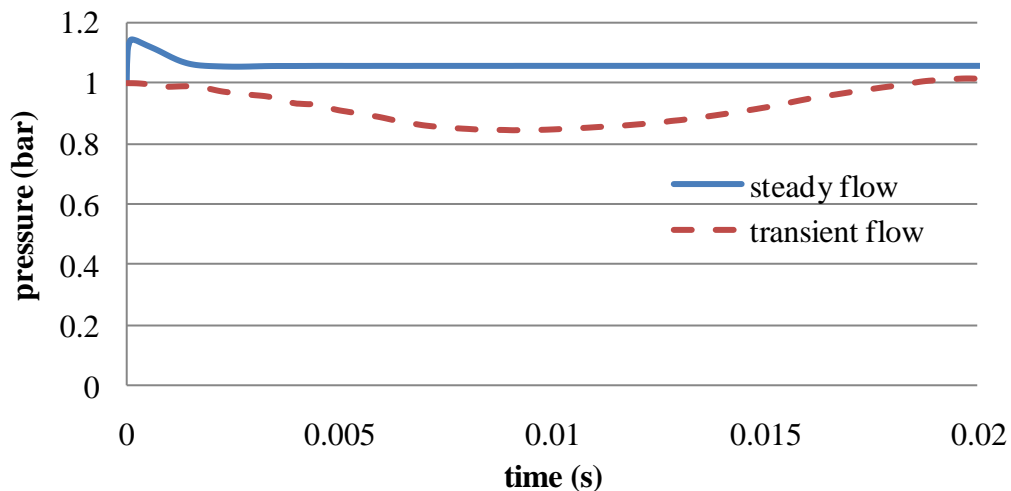


Figure 55 A comparison of intake port pressure between steady flow and transient flow

Second, the physical and mechanical conditions are different. In actual engines, the shape and movement of the piston as well as the movement of the valves influence the flow inside the cylinder. The air flow has stronger waves in the transient flow than in the steady flow. Third, the steady flow tests use air only, while the air and fuel mixing can occur in a real engine, which is significantly different.

CHAPTER 5

CONCLUSION

A preliminary study of the intake flow inside a cylinder is performed. The air motion inside the cylinder with a Yanmar NFD-170 cylinder head at 6 mm lift was modeled by the CONVERGE software and the experimental investigation was conducted using the LDA technique. The experiment setup facilitates the back-scattering LDA through the transparent cylinder. A dedicated generation method for water droplets was successfully applied for proper seeding of the flow during the LDA measurements. The flow analysis shows that the spatial in-cylinder flow structures can be achieved from a relatively small number of measurements. Comparisons of the steady state numerical and experimental results of the flow structure and flow velocity shows that the major features are successfully predicted. The agreement between the steady state simulation and experiment results validate the geometry and the flow models used. The RMS velocity scaled well with the mass flow rate.

The results show that the steady state flow simulation can predict primary flow directions which may be used to gain insight on the initial intake flow characteristics inside the cylinder. This method can be used to improve the in-cylinder air motion of engines before the complex and time consuming engine conditions are undertaken.

The next step of the investigation will include the moving piston and the dynamic valve lift profile. These parameters can be applied to quantify the evolution of the intake flow motion during the intake and compression strokes. In addition, other techniques, such as the PIV measurement may be applied to check the correlation of the flow structures with

the LDA results. In order to obtain a more complete flow description, the current used computational method need to be improved and other computational methods may also apply.

REFERENCES

1. Steady state. In Wikipedia. Accessed on 2013, February 8, from http://en.wikipedia.org/wiki/Steady_state
2. Transient state. In Wikipedia. Accessed on 2013, February 15, from http://en.wikipedia.org/wiki/Transient_state.
3. Z.Mahmood, A. Chen, M.Yianneskis and G.Ganti. On the structure of steady flow through dual-intake engine ports, King's College London, International Journal for Numerical Methods in Fluids, Vol. 23, 1085-1109
4. J M Desantes, J V Pastor and A Doudou. Study of the steady flow produced by direct injection diesel engine intake ports, Proceedings of the Institution of Mechanical Engineers, Part D: Journal of Automobile Engineering 2001 215: 285
5. L. John Lumley. Flow in the cylinder, Cornell University (excerpt from his book: Engines – an introduction. Cambridge University Press, 1999)
6. G J Micklow and W-D Gong. Intake and in-cylinder flowfield modeling of a four-valve diesel engine, East Carolina University, Greenville, North Carolina, USA, Proceedings of the Institution of Mechanical Engineers, Part D: Journal of Automobile Engineering 2007 221: 1425
7. M. Zahurul Haq. Volumetric Efficiency of Engines, Bangladesh University of Engineering & Technology, 2011
8. CONVERGE™: A Three-Dimensional Computational Fluid Dynamics Program for Transient or Steady State Flows with Complex Geometries (Version 1.3), Convergent Science Inc, March, 2008. CONVERGE manual

9. S.L. van den Heuvel, A.A. van Steenhoven and R.S.G. Baert. Three-dimensional calculations and laser velocimetry validation of steady-state port-Valve-cylinder flows, Department for Internal Combustion Engines, Eindhoven University of Technology, NL, 7th International Conference on Laser Anemometry
10. F.Payri, J. Benajes, X, Margot, A. Gil, CMT-Motores T_ermicos. CFD modeling of the in-cylinder flow in direct-injection diesel engines, Universidad Politecnica de Valencia, Camino de Vera s/n, 46022 Valencia, Spain
11. Laser Doppler anemometry-Introduction to principles and applications, published by Dantac Dynamics Company
12. Laser Doppler velocimetry. In Wikipedia. Accessed on 2013, February 25, from http://en.wikipedia.org/wiki/Laser_Doppler_velocimetry
13. Particle Image Velocimetry. In Velocimetry Knowledge United. Accessed on 2013, March 9, from <http://www.velocimetry.net/principle.htm>
14. Damian E. Ramajo, Norberto M.Nigro. Numerical and experimental in-cylinder flow study in a 4-valve spark ignition engine, INTEC-Universidad Nacional del Litoral-CONOCET, International Center for Computational Method in Engineering, November, 2008
15. Julie Vernet. Detailed study of steady in-cylinder flow and turbulence using stereo-PIV, SCANIA, Sweden, 2012
16. Measurement Principles of PIV. In Dantec Dynamics. Accessed on 2013, March 12, from <http://www.dantecdynamics.com/Default.aspx?ID=820>

APPENDIX A CONVERGE SIMULATION INPUT FILES LIST

The following files are required for all simulations

<i>Input files</i>	<i>File Description</i>
inputs.in	Main driver specifying various quantities including: simulation start time, end time, output frequency, physical model activation, solver settings and base grid size
initialize.in	Contains boundary condition information for each boundary zone specified in the preprocessor. This is also where regions are defined.
boundary.in	Used to provide initial conditions for each region of the domain
post.in	Defines which variables will be written out for 3D contour post processing.
surface.dat	Triangulated surface specification and boundary assignment.
events.in	Information about connecting and disconnecting regions.
engine.in	Inputs specific to an engine simulation.
therm.dat	NASA formatted data for calculating the thermodynamic properties of the species in the simulation.
gas.dat	Properties for the gas that cannot be calculated from the data in therm.dat.

APPENDIX B MATLAB CODES FOR CONTOUR PLOTS

```
clc
clear all
close all
listi=dir('*.*col');
chara={listi.name};

for i=1:n
cell_data=importdata(cell2mat(chara(i)));

first_col=cell2mat(cell_data.textdata(1));
asc= uint8(first_col);
CAD(i)=str2num(char(asc(1:14)));

X = [cell_data.data(:,1) cell_data.data(:,2) cell_data.data(:,3)];
newX=cell_data.data(find((cell_data.data(:,2))>
0.003&(cell_data.data(:,2))<0.003&(cell_data.data(:,3))<=0.000),1);
newZ=cell_data.data(find((cell_data.data(:,2))>-
0.003&(cell_data.data(:,2))<0.003&(cell_data.data(:,3))<=0.000),3);

u=cell_data.data(find((cell_data.data(:,2))>-
0.003&(cell_data.data(:,2))<0.003&(cell_data.data(:,3))<=0.000),5);
v=cell_data.data(find((cell_data.data(:,2))>-
0.003&(cell_data.data(:,2))<0.003&(cell_data.data(:,3))<=0.000),6);
w=cell_data.data(find((cell_data.data(:,2))>-
0.003&(cell_data.data(:,2))<0.003&(cell_data.data(:,3))<=0.000),7);

newY=sqrt((u.*u)+(v.*v)+(w.*w));
dx=min(newX):0.0001:max(newX);
dz=min(newZ):0.0001:max(newZ);
[qx,qz] = meshgrid(dx,dz);
qy = griddata(newX,newZ,newY,qx,qz);
clear newX newZ

% newX=cell_data.data(find((cell_data.data(:,3))>-0.054&(cell_data.data(:,3))<-0.05),1);
```

```

% newY=cell_data.data(find((cell_data.data(:,3))>-0.054&(cell_data.data(:,3))<-0.05),2);
% u=cell_data.data(find((cell_data.data(:,3))>-0.054&(cell_data.data(:,3))<-0.05),5);
% v=cell_data.data(find((cell_data.data(:,3))>-0.054&(cell_data.data(:,3))<-0.05),6);
% w=cell_data.data(find((cell_data.data(:,3))>-0.054&(cell_data.data(:,3))<-0.05),7);
% newZ=sqrt((u.*u)+(v.*v)+(w.*w));
% dx=min(newX):0.0001:max(newX);
% dy=min(newY):0.0001:max(newY);
% [qx,qy] = meshgrid(dx,dy);
% qz = griddata(newX,newY,newZ,qx,qy);
% clear newX newY

fig=figure(2);
set(fig, 'renderer', 'opengl')
%contourf(qx,qy,qz,100,'LineStyle','none');
contourf(qx,qz,qy,100,'LineStyle','none');
hold all
clear newqx newqz newqy

axis([-0.06 0.06 -0.11 0])
xlabel('X[m]')
ylabel('Z[m]')
text(0.04,0.005,'Velocity (m/s)')
CADD=sprintf('%d cycle',CAD(i));
text(-0.04,0.005,0.005,CADD)

colorbar
caxis([0 50])

end'

```


APPENDIX C MATLAB CODES FOR QUIVER PLOTS

```
clc
clear all
listi=dir('*.*col');
chara={listi.name};

for i=195
cell_data=importdata(cell2mat(chara(i)));

first_col=cell2mat(cell_data.textdata(1));
asc= uint8(first_col);
CAD(i)=str2num(char(asc(1:14)));

X = [cell_data.data(:,1) cell_data.data(:,2) cell_data.data(:,3)];
%
newX=cell_data.data(find((cell_data.data(:,2))>0.002&(cell_data.data(:,2))<0.002&(cell_data.data(:,3))<=
0),1);
%
newY=cell_data.data(find((cell_data.data(:,2))>0.002&(cell_data.data(:,2))<0.002&(cell_data.data(:,3))<=
0),2);
%
newZ=cell_data.data(find((cell_data.data(:,2))>0.002&(cell_data.data(:,2))<0.002&(cell_data.data(:,3))<=
0), 3);
%
u=cell_data.data(find((cell_data.data(:,2))>0.002&(cell_data.data(:,2))<0.002&(cell_data.data(:,3))<=0),5);
%
v=cell_data.data(find((cell_data.data(:,2))>0.002&(cell_data.data(:,2))<0.002&(cell_data.data(:,3))<=0),6);
%
w=cell_data.data(find((cell_data.data(:,2))>0.002&(cell_data.data(:,2))<0.002&(cell_data.data(:,3))<=0),7);
newX=cell_data.data(find((cell_data.data(:,3))>-0.012&(cell_data.data(:,3))<-0.01),1);
newY=cell_data.data(find((cell_data.data(:,3))>-0.012&(cell_data.data(:,3))<-0.01),2);
newZ=cell_data.data(find((cell_data.data(:,3))>-0.012&(cell_data.data(:,3))<-0.01),3);
u=cell_data.data(find((cell_data.data(:,3))>-0.012&(cell_data.data(:,3))<-0.01),5);
v=cell_data.data(find((cell_data.data(:,3))>-0.012&(cell_data.data(:,3))<-0.01),6);
w=cell_data.data(find((cell_data.data(:,3))>-0.012&(cell_data.data(:,3))<-0.01),7);
```

```

fig=figure(2);
set(fig, 'renderer', 'opengl')
quiver3(newX(1:5:end,1:5:end),newY(1:5:end,1:5:end),newZ(1:5:end,1:5:end),u(1:5:end,1:5:end),
        v(1:5:end,1:5:end),w(1:5:end,1:5:end),2,'color',[0 0 0])

hold on
view([0 90])
axis ([-0.06 0.06 -0.06 0.06 -0.11 0])

xlabel('X[m]');
ylabel('Y[m]');
zlabel('Z[m]');

CADD=sprintf('%d cycle',CAD(i));
text(-0.04,0.065,0.005,CADD)
end

```

VITA AUCTORIS

NAME: Qiaochu Han
PLACE OF BIRTH: Shenyang, China
YEAR OF BIRTH: 1989
EDUCATION: University of Windsor, B.Sc., Windsor, ON, 2011
University of Windsor, M.Sc., Windsor, ON, 2013